Data-driven Drell-Yan background determination for a search for supersymmetry in di-leptonic final states at CMS with LHC Run II data

von

Marius Teroerde

Masterarbeit in Physik

vorgelegt der

Fakultät für Mathematik, Informatik und Naturwissenschaften der RWTH Aachen

im

Oktober 2016

angefertigt im

I. Physikalischen Institut B

bei

Gutachter: Prof. Dr. Lutz Feld
Zweitgutachter: Prof. Dr. Stefan Schael

Aachen, Datum

CERN-THESIS-2016-194

Eidesstattliche Versicherung

______________________________ ______________________________

Name, Vorname Matrikelnummer (freiwillige Angabe)

Ich versichere hiermit an Eides Statt, dass ich die vorliegende Arbeit/Bachelorarbeit/ Masterarbeit* mit dem Titel

selbständig und ohne unzulässige fremde Hilfe erbracht habe. Ich habe keine anderen als die angegebenen Quellen und Hilfsmittel benutzt. Für den Fall, dass die Arbeit zusätzlich auf einem Datenträger eingereicht wird, erkläre ich, dass die schriftliche und die elektronische Form vollständig übereinstimmen. Die Arbeit hat in gleicher oder ähnlicher Form noch keiner Prüfungsbehörde vorgelegen.

Ort, Datum Unterschrift

*Nichtzutreffendes bitte streichen

Belehrung:

§ 156 StGB: Falsche Versicherung an Eides Statt

Wer vor einer zur Abnahme einer Versicherung an Eides Statt zuständigen Behörde eine solche Versicherung falsch abgibt oder unter Berufung auf eine solche Versicherung falsch aussagt, wird mit Freiheitsstrafe bis zu drei Jahren oder mit Geldstrafe bestraft.

§ 161 StGB: Fahrlässiger Falscheid; fahrlässige falsche Versicherung an Eides Statt

(1) Wenn eine der in den §§ 154 bis 156 bezeichneten Handlungen aus Fahrlässigkeit begangen worden ist, so tritt Freiheitsstrafe bis zu einem Jahr oder Geldstrafe ein.

(2) Straflosigkeit tritt ein, wenn der Täter die falsche Angabe rechtzeitig berichtigt. Die Vorschriften des § 158 Abs. 2 und 3 gelten entsprechend.

Die vorstehende Belehrung habe ich zur Kenntnis genommen:

Ort, Datum Unterschrift

Contents

1 Introduction **5**

2 Theory **7**
2.1 Standard Model of Particle Physics . . . 7
2.1.1 Hierarchy Problem . . . 9
2.1.2 Dark Matter . . . 9
2.2 Supersymmetry . . . 10
2.2.1 R-Parity Conservation . . . 10
2.2.2 Consequences of SUSY in Nature . . . 11
2.2.3 Considered SUSY Model . . . 11

3 Experimental Setup **13**
3.1 Large Hadron Collider . . . 13
3.2 The CMS detector . . . 14
3.2.1 Inner Tracking System . . . 15
3.2.2 Electromagnetic Calorimeter . . . 16
3.2.3 Hadron Calorimeter . . . 16
3.2.4 Superconducting Solenoid . . . 17
3.2.5 Muon System . . . 17
3.2.6 Trigger System . . . 18

4 Event Reconstruction and Selection **19**
4.1 Dataset . . . 19
4.2 Simulation and Software . . . 19
4.3 Reconstruction of Physics Objects . . . 20
4.3.1 Primary Vertex . . . 21
4.3.2 Electrons . . . 21
4.3.3 Muons . . . 22
4.3.4 Jets . . . 22
4.3.5 Missing Transverse Energy . . . 23
4.4 Event Selection . . . 23

5 Signal Regions **24**
5.1 Search in 2015 . . . 24
5.2 Search in 2016 . . . 24
5.3 Standard Model Backgrounds . . . 25

6 Background Estimation **27**
6.1 Flavor-Symmetric Backgrounds . . . 27

6.2 Drell-Yan like processes 30
6.2.1 The Jet-Z Balance method 31
6.2.2 E_T^{miss}-Template Method 49
6.3 Other Backgrounds 50

7 Results **51**
7.1 Estimation of Z+jets events in signal region for the 2015 search 51
7.2 Background estimation in the signal region for the 2016 search 52

8 Summary and Outlook **55**

A List of used Datasets **56**

B Simulated Datasets **59**

1 Introduction

The current understanding of elementary particle physics is best described by the Standard Model of particle physics (SM). This model is a mathematical way to characterize particles and interactions between particles. The SM postulates the existence of 17 elementary particles of which every single one has been discovered, the newest addition being the Higgs Boson which was discovered in 2012 [1, 2]. The predictions made by the SM have been confirmed with high precision in various measurements, for example measurements of the Z [3] and W [4] boson masses and widths. Despite the success of the SM, it has characteristics that are deemed unnatural such as the hierarchy problem and the SM gives no explanation for the occurence of dark matter. This suggests that the SM is not complete.

Many theoretical models that extend the SM have been developed in order to explain unexplained phenomena. As these models often predict minor effects that are hard to measure, high precision measurements and sophisticated searches for physics beyond the SM have to be performed in order to be able to confirm or falsify these models. The CERN Large Hadron Collider (LHC) and its detectors provide the infrastructure for these measurements.

A popular example for theories beyond the SM are supersymmetric (SUSY) models. In these models, partner particles of the SM particles exists. In many SUSY models, the lightest SUSY particle is stable and neutral, so it cannot be detected. This is a clear signature in measurements and can be used for the detection of SUSY. In general, SUSY models are expected to create excesses over the SM expectation in certain distributions.

In data taken by the Compact Muon Solenoid (CMS) at $\sqrt{s} = 8\,\text{TeV}$ in 2012, an excess over SM expectation with a significance of $2.6\,\sigma$ [5] was found in the invariant dilepton mass spectrum at 70 GeV. A fit to the dileptonic mass spectrum (Fig. 1) shows an edge-like signal structure with a significance of $2.4\,\sigma$. In a follow-up search in 2015 [6], the CMS collaboration found no significant excess over SM expectation in this signal region.

This excess was not confirmed by the ATLAS collaboration, which however reported an excess over SM expectation with a significance of $3\,\sigma$ [7] in events with a dileptonic mass compatible with Z bosons. An excess in the same signal region was found by ATLAS in data taken in 2015, this time with a significance of $2.2\,\sigma$ [8].

The aim of this thesis is to establish the Jet-Z Balance (JZB) method, which is a data-driven estimation method for the Drell-Yan process. The JZB variable, which is the difference between hadronic recoil and the transverse momentum of the dilepton system, is symmetric around zero for Drell-Yan events. As events from SUSY processes with undetected particles are more likely to have positive values of JZB, a control region depleted of SUSY events can be defined for the estimation of the Drell-Yan background. This estimation is used as a statistically independent validation of the Drell-Yan back-

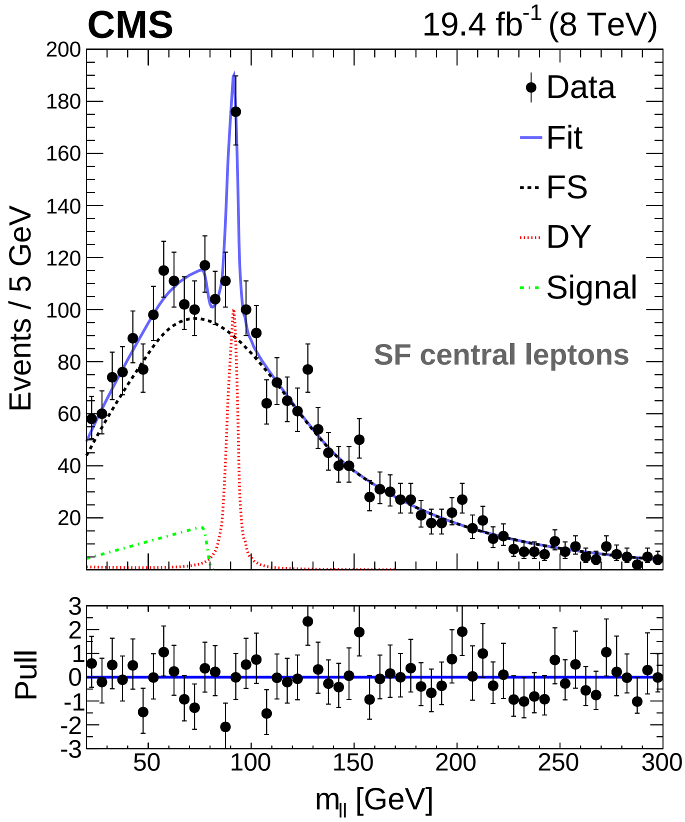

Figure 1: Kinematic fit in the dileptonic mass spectrum which yields an excess over SM expectation with a significance of $2.4\,\sigma$ [5].

ground estimation on data taken by the CMS detector in 2015. Additionally, a search for physics beyond the Standard Model based on the JZB method is developed and carried out on data taken in 2016 in order to probe whether the excess found by the ATLAS collaboration is a statistical fluctuation or a possible hint at physics beyond the Standard Model.

2 Theory

For simplicity, the natural unit system is used throughout this thesis, setting the reduced Planck constant and the speed of light to 1:

$$\hbar = c = 1$$

In this unit system particle masses, momenta, and energies are given in GeV. This unit system is not used for other observables, thus lengths are measured in meters and cross sections are measured in barn ($1\,\mathrm{b} = 10^{-28}\,\mathrm{m}$). Integrated luminosities are given in b^{-1}.

2.1 Standard Model of Particle Physics

The Standard Model of Particle Physics (SM) is a theoretical model describing the interactions between elementary particles. It is implemented as a renormalizable quantum field theory [9–13]. Fundamental forces are derived as a result of symmetries.

The gauge group describing all SM interactions is

$$\mathrm{SU}(3) \times \mathrm{SU}_L(2) \times \mathrm{U}_Y(1). \tag{2.1}$$

Here, the SU(3) component represents the strong force, which is implemented in the theory of Quantum Chromodynamics (QCD). The $\mathrm{SU}_L(2)\times\mathrm{U}_Y(1)$ component describes electroweak interactions, a unified theory of electromagnetic and weak interactions.

The particle content [14] of the SM is summarized in Fig. 2.

All particles can be classified as half-integer spin particles called fermions and integer spin particles called bosons. Fermions are further subdivided into quarks and leptons, while bosons are divided into gauge bosons and the Higgs boson.

Leptons and Quarks are sorted into three generations. Each generation of leptons consists of one electrically charged lepton carrying one negative elementary charge ($-e$) and one associated electrically neutral lepton called neutrino. Compared to the charged leptons, neutrinos have a very small mass. This mass is zero in the SM, as the nature of neutrino mass is not yet clear. Each lepton has a lepton number of 1. This number is found to be conserved in the SM, but there is no explicit conservation postulated.

Each quark generation is constituted of one "up-type" quark with an electric charge of $2/3\,e$ and a "down-type" quark with charge $-1/3\,e$. Thus, the existing quark flavors are up and down, charm and strange, and top and bottom. Quarks have a baryon number of 1/3, the baryon number is empirically also a conserved quantity.

All fermions have antiparticles with opposite electrical charges and negative lepton/baryon numbers but otherwise same quantum numbers and masses. Antiparticles are denoted with a "+" (charged leptons, for example e^+) or by a bar (all other fermions,

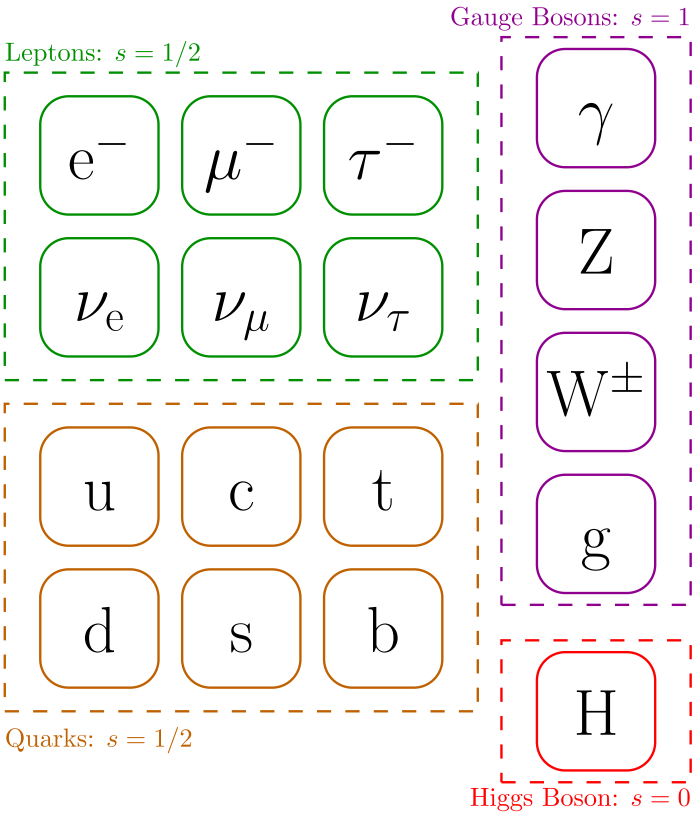

Figure 2: Particle content of the Standard Model

for example $\bar{t}$). Fermions of higher generations also have higher particle masses.

The four gauge bosons are the force mediating particles of the standard model. They have a spin of 1 and are the quanta of their respective gauge fields.

The photon (γ) is the mediator of the electromagnetic force. It interacts with electrically charged particles but is electrically neutral, so there is no direct self-interaction.

The W and Z bosons mediate the weak force and are the only massive gauge bosons. While the Z boson is electrically neutral, the $W^\pm$ bosons have a charge of $\pm e$. For $W^\pm$ interactions, the concept of helicity is important. Helicity describes the direction of a particle's spin with respect to its direction of movement. If the spin direction is in the direction of movement, the particle's helicity is "right-handed" while in the opposite case the particle's helicity is "left-handed". The W bosons only interact with particles that have left-handed helicity and antiparticles that have right-handed helicity. This is important as neutrinos with right-handed helicity do not exist according to the SM.

The gluon is the mediator of the strong force which is based on three different color charges. The gluon carries a color-anticolor charge combination, meaning that there are eight possible color charges for a gluon. The gluon couples to particles with color charge, namely other gluons and quarks. The strong force has the special property that a particle with non-neutral color charge cannot be isolated. This property, called confinement, causes color-charged singular particles to be unstable, so that only particles or particle compounds with neutral color charge can be stable. The first possibility for stable compound particles formed by quarks are baryons, composed of three quarks that carry the colors red, green and blue, which combine to a color neutral state. The second possible configuration are mesons, which are formed by a quark and an antiquark, so that a color and an anticolor compensate each other to achieve a neutral color charge. Combinations of these states are in principle also possible.

Because of the confinement of color charged particles, quarks and gluons created or scattered in interactions cannot be isolated. This leads to the pair creation of additional quarks and gluons when two confined particles are moving away from each other. As a result, highly energetic, cone-shaped showers of electrically charged and neutral hadrons ("jets") and their decay products are produced. This process is called "hadronization".

The Higgs boson is the latest addition to the SM and is the first fundamental particle with a spin of 0. It was found in 2012 by the ATLAS [2] and CMS [1] collaborations and has a mass of $125.7 \pm 0.4\,\text{GeV}$. The electrically and color neutral particle is an excitation of a component of the Higgs field, which was introduced into the SM in order to allow massive gauge bosons while still preserving local gauge invariance. The Higgs mechanism [15, 16] also gives masses to the fermionic particles. While the discovery of the Higgs boson was an important success in completing the SM, the Higgs mechanism does not directly predict any particle masses, as these are just parameters in the coupling to the Higgs boson. The SM including the Higgs mechanism does not describe gravity.

2.1.1 Hierarchy Problem

One major issue with the SM is the hierarchy problem [17]. At the Planck scale, gravitational effects cannot be neglected. While new physics might exist at a lower energy scale, this is the highest energy scale up to which the SM in its current form can be valid and new physics is to be expected. Because of loop corrections to the Higgs boson mass, m_{H}^2 gets corrections that go quadratically with this energy scale. For the Higgs boson to have the observed mass, these corrections have to cancel out with the tree-level Higgs boson mass. This is considered very unnatural by many theorists as the corrections at Planck scale would be of the order $10^{38}\,\text{GeV}^2$. As the quadratic Higgs boson mass is measured to be at energies of about $10^4\,\text{GeV}^2$, the cancellation with the tree-level Higgs boson mass has to happen to a precision of 10^{34}.

2.1.2 Dark Matter

When observing the rotational velocity of stars and gas around their galaxy centers, an anomaly is observed: While the velocity is expected to fall off for larger rotation radii, it is constant. The measured velocity can be explained if a halo of invisible, but gravitating matter (dark matter) exists around the galaxy [18]. Additional evidence is found in the anisotropies of the cosmic microwave background which cannot be explained without dark matter [19]. It is largely assumed that dark matter is not composed of baryonic matter or neutrinos [20], suggesting the existence of at least one non-SM particle that is neutral, stable and only interacts weakly.

2.2 Supersymmetry

Supersymmetric (SUSY) models [17] are popular extensions to the SM. In these models, each SM particle has one partner particle with identical quantum numbers except for the spin, which is different by 1/2. This means that each fermion gets a boson superpartner (sfermion) and each boson gets a fermion superpartner (bosino). Supersymmetric particles are labeled with a tilde on top of their symbol (e.g. $\tilde{\mathrm{l}}$) and are named after their SM equivalent with a prefix "s" (for sfermions) or a suffix "ino" (for bosinos).

One supersymmetric model is the Minimal Supersymmetric Standard Model (MSSM) which implements SUSY with a minimum number of new particles. As the electroweak gauginos and the Higgsinos (two Higgs doublets are needed in the MSSM) have a spin of 1/2, they have identical quantum numbers. This allows for a mixing between these particles, resulting in the chargino pair $\tilde{\chi}^{\pm}_{1/2}$ and four neutralinos $\tilde{\chi}^{0}_{1/2/3/4}$ of which $\tilde{\chi}^{0}_{1}$ is the lightest and $\tilde{\chi}^{0}_{4}$ is the heaviest neutralino. The MSSM is the model used in this thesis.

Since no SUSY particle has been found, the symmetry (if realized in nature) has to be broken, giving the superpartner particles different masses than the original particles. There are several different possible breaking mechanisms resulting in different interactions. One example of models with SUSY breaking is gauge mediated supersymmetry breaking, in which gauge interactions are "messengers" of SUSY breaking, which happens in a "hidden" sector [17, 21]. In the GMSB view, not the breaking mechanism itself, but the way it is mediated, determines the way that SUSY interactions behave.

2.2.1 R-Parity Conservation

An important symmetry explicitly assumed in many SUSY models is R-parity conservation. Even though it is not explicitly assumed, the baryon number and the lepton number are conserved in the SM. This is not necessarily true for SUSY models, where in principle, conversions between fermions and bosons are allowed. However, these models are disfavored as the effects of a violation of this conservation would be observable. Therefore, R-parity, which incorporates the lepton and baryon numbers, is introduced:

$$P_R = (-1)^{3(B-L)+2s} \tag{2.2}$$

Here, B is the baryon number, L is the lepton number and s is the spin of a considered system. An important note about R-parity conservation is that all SUSY particles have the property $P_R = -1$ while all SM particles have $P_R = 1$. Therefore, R-parity conservation results in SUSY particles being produced in pairs as well as the lightest supersymmetric particle (LSP) being stable. In many models, the LSP is the $\tilde{\chi}_1^0$ particle.

2.2.2 Consequences of SUSY in Nature

Besides a number of new particles and interactions, a SUSY theory realized in nature could solve certain problems of the SM. The hierarchy problem can be solved by a SUSY theory as the first-order loop corrections to the Higgs boson mass from all particles cancel out with the corrections from their superpartner particles. This is not fully the case for higher-order corrections for a broken symmetry, however. In this case, SUSY particle masses cannot be too high, elsewise a new little hierarchy problem is introduced.

If R-parity is assumed as a conserved quantity, the LSP is stable. If this particle is an electrically neutral particle like the lightest neutralino, it is a candidate for dark matter since it only interacts through weak force interactions and gravity.

2.2.3 Considered SUSY Model

As the MSSM introduces more than 100 additional free parameters, it is hard to interpret obtained results in the context of the full MSSM. In order to reduce the number of free parameters, a so-called Simplified Model [22] approach is used. Models designed with this approach contain only a few new particles and interactions and concentrate on one process. In this way, results can be more easily interpreted and give meaningful interpretations for models with similar topologies.

In the context of this thesis, the "T6bbllslepton" (Fig. 3) scenario is relevant. It describes the pair production of a $\tilde{\mathrm{b}}$ quark which decays into a b quark and a $\tilde{\chi}_2^0$. The $\tilde{\chi}_2^0$ can decay into a lepton and a $\tilde{\mathrm{l}}$ ($\tilde{\mathrm{e}}$ or $\tilde{\mu}$), which in turn decays into a lepton and a $\tilde{\chi}_1^0$. Another possibility is for the $\tilde{\chi}_2^0$ to decay into a Z boson and a $\tilde{\chi}_1^0$. Depending on the mass difference between $\tilde{\chi}_2^0$ and $\tilde{\chi}_1^0$, the Z boson can be on- or off-shell. In this model, the $\tilde{\chi}_1^0$ is the LSP.

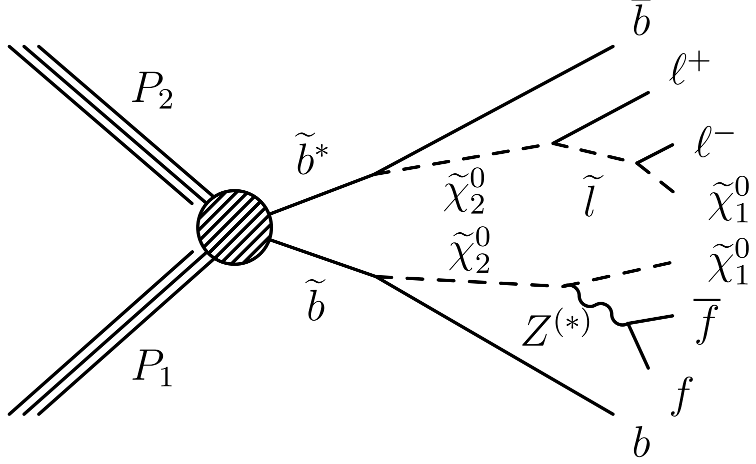

Figure 3: Feynman diagram of the “T6bbllslepton” model

This model is interesting considering the excess in the dileptonic mass spectrum described above as the $\tilde{\chi}_2^0$ decay via the intermediate slepton would result in an edge-like mass distribution of the dileptonic system. This could explain the previously mentioned excess found by CMS [5].

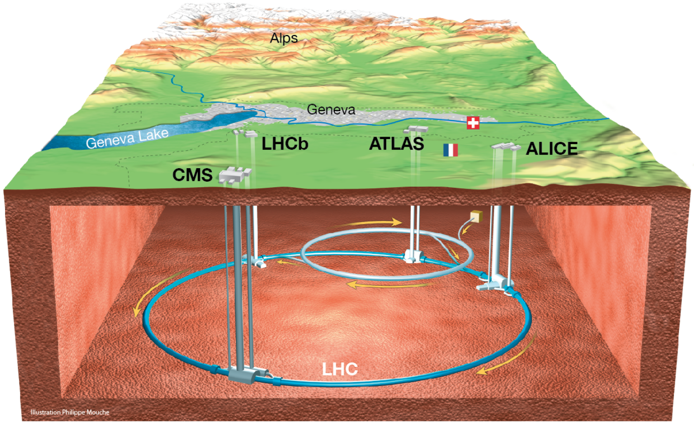

Figure 4: Schematic of the LHC and its detectors [25].

3 Experimental Setup

3.1 Large Hadron Collider

The Large Hadron Collider (LHC) [23] (Fig. 4) is located near the facilities of the European Organization for Nuclear Research (CERN). It is a synchrotron particle accelerator built in the already existing tunnel of the Large Electron Positron Collider (LEP) [24]. The accelerator has a circumference of 26.7 km and is located between 45 and 170 m below the surface.

As the LHC is designed for the acceleration of protons and lead ions, it has two separate beam pipes to accelerate the hadrons in opposite directions. At eight points, the beam pipes cross allowing for collisions between particles in the pipes. At four of these points, the most important particle detectors of the LHC are installed, namely the "A Toroidal LHC Apparatus" (ATLAS) [26] detector, the "Compact Muon Solenoid" (CMS) [27] detector, the "LHC beauty" (LHCb) [28] detector, and the "A Large Ion Collider Experiment" (ALICE) [29] detector. These detectors are built with different design philosophies. While ATLAS and CMS are multi-purpose detectors, LHCb is constructed as a device for precision measurements of c and b-quark decays and CP violation, and ALICE focusses on strongly interacting matter as well as the formation of quark-gluon plasmas.

Before entering the LHC, protons are preaccelerated to an energy of 450 GeV in an acceleration chain consisting of Linac2, the Proton Synchrotron Booster (PSB), the Proton Synchrotron (PS), and the Super Proton Synchrotron (SPS).

The design collision energy of the LHC machine for proton collisions is 14 TeV, with an individual beam energy of 7 TeV. While the LHC reached collision energies of 8 TeV in 2012, it came closer to its design value with a collision energy of 13 TeV in 2015 and maintained this energy in 2016. For proton collisions at ATLAS and CMS, the LHC aims at a design luminosity of $L = 10^{34}\,\mathrm{cm}^2\mathrm{s}^{-1}$ which was achieved and exceeded in June 2016 [30].

3.2 The CMS detector

The CMS detector [27] is a multi-purpose detector located at the LHC. Its defining features are a superconducting solenoid that generates a magnetic field of 3.8 T as well as the muon detection system. The cylindrical detector covers most of the 4π solid angle around the collision point (except for the beam pipe), using different subdetector layers to detect produced particles. The CMS detector is shown in Fig. 5.

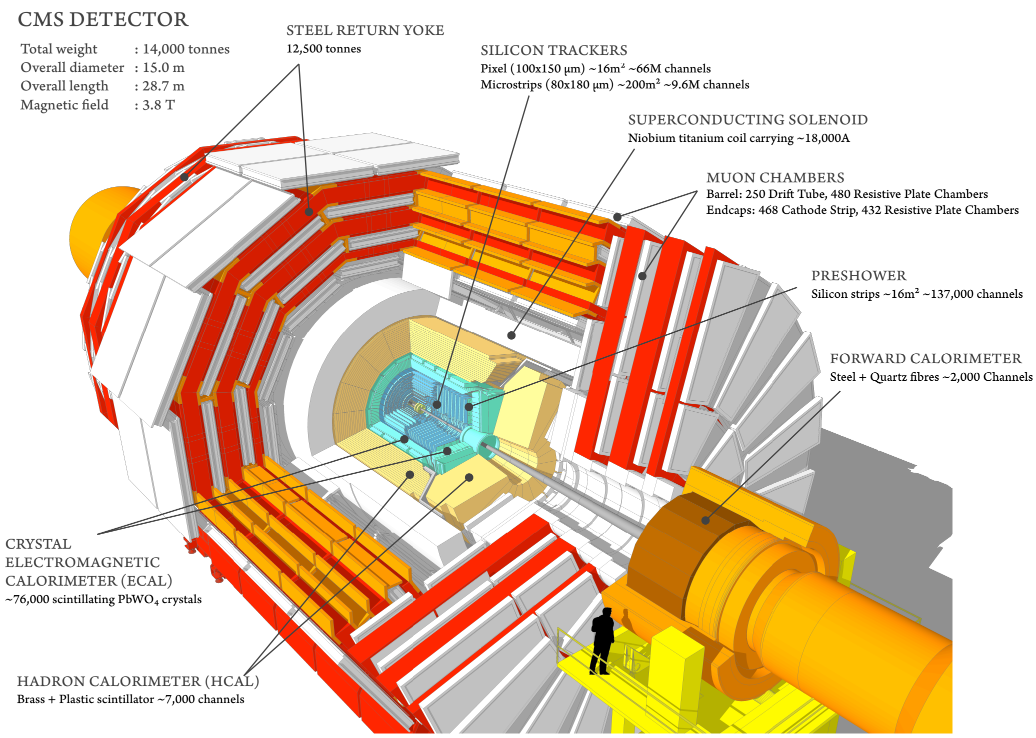

Figure 5: View of the CMS detector [31]

The coordinate system of CMS is centered at the nominal point of collision. The y-axis points upward, while the x-axis points horizontally to the center of the accelerator ring. Finally, the z-axis points in beam direction so that a right-handed coordinate system is established (anticlockwise). To use the symmetries of the detector and to introduce more easily interpretable coordinates, the azimuthal angle ϕ (measured from the x-axis in the x-y-plane) and the polar angle θ (measured from the z-axis) are introduced. The radial distance from the collision point is denoted as r. The pseudorapidity $\eta = -\ln\tan(\theta/2)$ is introduced as any $\Delta\eta = \eta_1 - \eta_2$ is invariant under Lorentz transformations in z-direction. Many variables are defined in the x-y-plane, which is the transverse plane, only. This is done because the center of mass of collisions is boosted in z direction, but not in the transverse plane. Some important variables are the transverse momentum of an object $p_T = \vec{p}\sin\theta$ and the hadronic activity $H_T = \sum_{\text{jets}} p_T$,

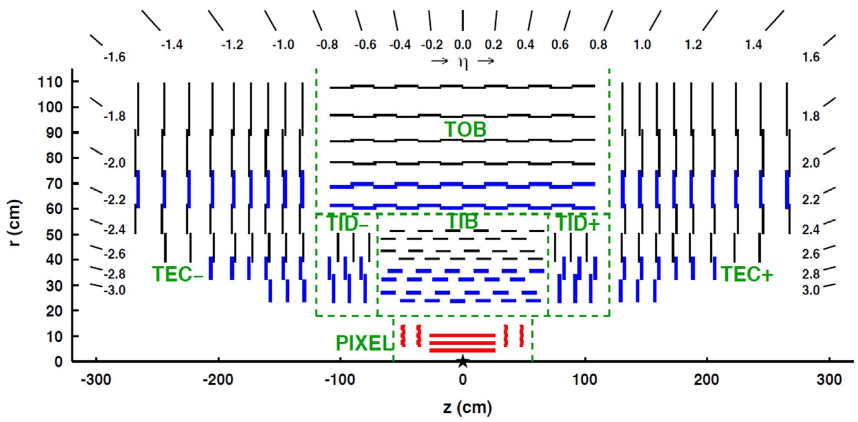

Figure 6: Layout of the inner tracking system of CMS [27].

which is the sum of the transverse momenta of all jets. As a measure of distance between two objects in the detector, $\Delta R = \sqrt{(\Delta\eta)^2 + (\Delta\phi)^2}$ is often used.

Close to the beam pipe, the inner particle tracking system is installed. The next layer is the electromagnetic calorimeter (ECAL), followed by the hadronic calorimeter (HCAL). All of these layers are enclosed by the superconducting solenoid. The outermost layer is made of the iron return yoke of the magnet in which different muon chambers are embedded.

3.2.1 Inner Tracking System

The inner tracking system of the CMS detector is composed of a silicon pixel tracker and a silicon strip tracker. With a diameter of 2.5 m and a length of 5.8 m it consitutes the innermost part of the detector. Covering areas up to a pseudorapidity of $\eta = \pm 2.5$, it was designed to reconstruct trajectories of charged particles inside the detector. This is done by semi-conductor technology that sends electrical signals upon a charged particle passing through.

The tracker layout is shown in Fig. 6. The pixel tracker as well as the strip tracker are divided into layers parallel to the beam pipe (barrel) and layers orthogonal to the beam pipe (endcaps). The pixel tracker consists of three 53 cm-long barrel layers (the closest at a radius of 4.4 cm) and two endcap layers at each side of the barrel at the positions $z = \pm 34.5$ cm and $z = \pm 46.5$ cm. Each pixel has a size of $100 \times 150\,\mu\text{m}^2$. This arrangement of overall 66 million pixels ensures a consistent resolution only weakly dependent on the track direction.

The silicon strip tracker is divided into an inner and an outer part. The tracker inner barrel (TIB) consists of four strip layers while on each side of the barrel, three disks of strips (TID) are positioned. The inner part extends up to a radius of 55 cm. The outer part of the detector consists of six barrel layers (TOB) and nine disk endcap layers (TEC).

The tracking system was designed to provide a high granularity and is able to reliably distinguish charged particle tracks even at high instantaneous luminosities. The precise track reconstruction is also essential for the reconstruction of interaction vertices. The momentum resolution for particles at about $p = 100\,\mathrm{GeV}$ is $1 - 2\,\%$, decreasing with higher momenta due to a smaller curvature and decreasing for pseudorapidities greater than $|\eta| = 1.6$ due to a decreased lever arm.

3.2.2 Electromagnetic Calorimeter

The ECAL is the second subdetector layer of the CMS detector and measures the energy of electromagnetically interacting particles. The ECAL is based on lead tungstate crystals. A particle passing through the crystals loses energy, causing the crystals to scintillate which generates photonic showers. The visible light is then detected by photodetectors. Lead tungstate was chosen because of the high density, short radiation length and small Molière radius, making it possible to keep the ECAL as compact as possible while still obtaining a high granularity. Each crystal has a length of 23 cm, which is equivalent to 25.8 radiation lengths. A total pseudorapidity range of $|\eta| < 3$ is covered by the ECAL, with a transition between barrel and endcaps at $|\eta| = 1.479$.

The energy resolution achieved by the ECAL is of the form

$$\left(\frac{\sigma}{E\,[\mathrm{GeV}]}\right)^2 = \left(\frac{S}{\sqrt{E\,[\mathrm{GeV}]}}\right)^2 + \left(\frac{N}{E\,[\mathrm{GeV}]}\right)^2 + C^2. \tag{3.1}$$

Here, S is a stochastic term which covers different uncertainties from fluctuation, N is the noise term from electronic as well as pileup noise and C is a constant term covering uncertainty sources such as energy leakage and intercalibration errors. In test beam experiments, the terms were found to be $S = 2.8\,\%$, $N = 0.12$ and $C = 0.30\,\%$. In these test runs, an energy resolution of about $0.5\,\%$ was achieved for 120 GeV electrons.

3.2.3 Hadron Calorimeter

The hadron calorimeter is an important device for the measurement of jets which are important for many event signatures. Constrained by the ECAL ($R = 1.77\,\mathrm{m}$) and the magnetic coil ($R = 2.95\,\mathrm{m}$), the hadron barrel (HB) covers pseudorapidities up to $|\eta| < 1.3$. To provide enough stopping power for the measurement of jets, the outer hadron calorimeter (HO) is implemented outside the superconducting solenoid. The HB is composed of alternating layers of brass or steel and a plastic scintillator. By this principle the brass/steel layers absorb particle energies, causing showers, which then create light in the scintillator material. This light is read out with the help of light conducting fibers. The HO works in a similar way, also using the solenoid as an absorber. It is structered similarly to the HB to provide comparable resolutions.

Pseudorapidities between $1.3 < |\eta| < 3.0$ are covered by the hadron endcap (HE). It uses the same detection priniciple as the HB and HO, though its granularity is worse for $|\eta| > 1.6$. To cover large pseudorapidities up to $|\eta| < 5.2$, an additional hadron forward (HF) detector is used. To achieve a high radiation hardness (due to large energies being deposited in this region), the HF is composed of quartz fibers. Particles passing through emit cherenkov radiation, which is detected by photomultipliers.

3.2.4 Superconducting Solenoid

To bend the trajectories of charged particles and allow the determination of their momenta in the tracking system and the muon chambers, the superconducting solenoid was designed. The NbTi magnet, which measures 12.5 m in length and 6 m in diameter generates a magnetic field of 3.8 T. For this purpose, it is cooled down to 4.5 K.

3.2.5 Muon System

The Muon System is the outermost layer of the CMS detector. As all other (detectable) particles are absorbed in the previous layers, only muons escape the detector. Due to the resulting low background and the clear signature of muons, an efficient measurement is possible. To detect and measure muons, three different types of gaseous detectors are used. The barrel drift tubes (DT) are integrated between layers of the return yoke and cover a pseudorapidity range of $|\eta| < 1.2$. It is structured in four stations of which three measure the r-ϕ coordinates as well as the z coordinate of a passing muon and one station that only measures the r-ϕ coordinates. The endcap regions ($0.9 < |\eta| < 2.4$) are covered by cathode strip chambers (CSC) which are positioned perpendicular to the beam pipe. As the muon rate as well as the background in this region are higher, the CSC were implemented because of their fast response time and their radiation hardness.

Except for the regions around gaps between DT wheels and transition points at $|\eta| = 0.25$, $|\eta| = 0.8$ and $|\eta| = 1.2$, the reconstruction efficiency is consistently greater than 95 %. Combined with the inner tracker measurement, muon transverse momenta can be measured with an uncertainty between 5 and 15 % (depending on pseudorapidity) even at high muon momenta of 1 TeV. For muon transverse momenta below 100 GeV, the resolution is between 1 and 6 % depending on pseudorapidity [32].

A third type of muon detectors, composed of resistive plate chambers (RPC), is implemented. This system is solely used for triggering events with muons and provides fast response and good time resolution, thus being suitable for triggering at high rates. In total there are six layers of RPCs implemented in the muon system, covering pseudorapidities up to $|\eta| = 1.6$.

3.2.6 Trigger System

As the bunch crossings at CMS happen at rates of 40 MHz it is not feasible to record every collision as the resulting data load would be impossible to store and process. To reduce the rate of data while still maintaining as many interesting events as possible, a two-level trigger system is used. This system consists of the electronics-based level-1 triggers (L1) and the software-based high-level triggers (HLT).

As a L1 trigger needs to be fast, it only has access to coarse information from the subdetectors to identify a general event signature. The L1 trigger system can be grouped in local, regional and global triggers. Local triggers use primitive information of energy deposits in calorimeters and hits in the muon chambers. Regional triggers combine this information to identify trigger objects such as electron and muon candidates, while also giving a confidence level of the measurements. Global triggers combine all available information and decide whether an event is passed on the HLT system. The L1 trigger thereby reduces the event rate to about 100 kHz.

The HLT has access to the complete read-out data and thus can put further constraints on events, reducing the rates to an order of 1 kHz. To avoid too high events rates, the thresholds for both L1 trigger and HLT are readjusted during the data taking depending on the current instantaneous luminosity.

4 Event Reconstruction and Selection

4.1 Dataset

In this work, data taken at CMS in 2015 and 2016 at a center-of-mass energy of $\sqrt{s} = 13\,\text{TeV}$ are used. For the 2015 analysis, $2.3\,\text{fb}^{-1}$ of data are used. The 2016 analysis was published using $12.9\,\text{fb}^{-1}$ of data, which is the dataset that was used for ICHEP 2016 [33] publications. The used dilepton triggers of both years can be found in Appendix A.

4.2 Simulation and Software

In order to be able to control the background estimation methods, samples of relevant SM processes and their resulting interactions in the detector are simulated. Using the simulated samples, one can look at kinematic distributions in different selections to predict the behavior of data. In contrast to other analyses, this work mostly does not rely on simulation to directly predict the contribution of SM backgrounds and instead uses data-driven estimation methods for the most relevant processes, thus simulated samples are mostly used for validation. It is also possible to simulate SUSY processes to understand how possible SUSY signals would appear in data and to interpret the final results.

The simulation is performed in several steps. First, the specific process is simulated with an event generator. Depending on the process, either MadGraph [34, 35] or POWHEG [36–38] are used for the generation. To calculate the total cross section of a process, the matrix element of the process is calculated and convolved with parton distribution functions (PDFs) [39]. The PDFs are probabilistic functions derived at previous experiments and phenomenologically describe the inner structure of protons with regard to the energy carried by certain partons inside them. The calculated cross section can later be used to scale the simulated process to a certain luminosity which allows the generation of a high number of events while still being able to compare the simulation to data.

Secondly, parton showers are simulated. This is done with PYTHIA 8 [40]. These parton showers are results of hadronization and are not fully understood, so they are described phenomenologically.

The third step of simulation is to simulate the interaction of particles of each event with the detector material which results in the detector response. A detailed description of the CMS detector was implemented with Geant4 [41], which allows for a full emulation of the detection process. This includes simulating triggers for the samples generated for the dataset of 2015. As this step is very time consuming, it is only used for processes which are well known and where an imperfect description of the detector response could result in large uncertainties. For SUSY signal samples, theoretical uncertainties on the process are usually dominant and thus the FASTSIM [42] package is used for this step. The FASTSIM package uses a simplified description of the detector and achieves a simulation of the detector response and event reconstruction that is up to 100 times faster than using the full simulation with Geant4. Most resulting distributions of observables are compatible with the full simulation within a few percent, differences are accounted for by rescaling the FASTSIM generated samples.

The fourth step simulates the influence of pileup on each event. This includes in-time pileup from multiple interactions during a bunch crossing and out-of-time pileup from adjacent bunch crossings. To account for pileup, simulated minimum bias events are used. These events are representative of an average collision in the CMS detector and are tuned with events recorded in special runs. Each simulated event is overlaid with a number of minimum bias events so the distribution of the number of vertices in events matches the expected distribution in data. Differences between data and simulation are accounted for by reweighting the simulation.

The most important samples for this work are simulations of the Drell-Yan process [43] for which a data-driven estimation method is developed in this thesis. The samples for this process are binned in different categories of hadronic activity H_T. Simulating a high number of events with a certain hadronic activity serves the purpose of obtaining high statistical significance for events with high jet multiplicities, which are rare for the Drell-Yan process. With this method, a statistically saturated description of Drell-Yan events with high jet multiplicities is achieved.

Simulations of the simplified SUSY model "T6bbllslepton" with different $\tilde{b}$ and $\tilde{\chi}_2^0$ masses are used. For the mass scan, the $\tilde{b}$ mass is varied between 400 and 950 GeV while $\tilde{\chi}_2^0$ mass is varied between 150 GeV and the $\tilde{b}$ mass. The mass scan is done in 25 GeV steps for $\tilde{b}$ masses up to 800 GeV and in 50 GeV steps for higher masses. The $\tilde{\chi}_1^0$ mass is fixed at 100 GeV while the $\tilde{\text{l}}$ mass is set to $\frac{1}{2}(m_{\tilde{\chi}_2^0} + m_{\tilde{\chi}_1^0})$.

The simulation of the used samples is done centrally by CMS and is distributed as Minimal Analysis Object Data (Mini-AOD) [44] files that include information about the detector response as well as generator information of each event. The same file format is also used for the data samples, these however do not have any generator information. The Mini-AOD files are then processed using the CMS software (CMSSW) framework and are used locally as ROOT [45] trees that contain all necessary variables. The used simulated samples are listed in Appendix B.

4.3 Reconstruction of Physics Objects

Physical objects are reconstructed by the Particle Flow (PF) algorithm [46] using all subdetector information. As multiple proton-proton interactions happen at once (pileup), this includes defining a primary interaction vertex and identifying energy depositions from secondary interactions. Different physics objects relevant for this work are reconstructed as follows.

4.3.1 Primary Vertex

The primary interaction of a bunch crossing is found by clustering charged tracks into vertices [47,48] with the help of vertex reconstruction algorithms. The vertex with the largest p_T^2 sum of all reconstructed vertices is defined as the primary vertex and has to be reconstructed within 24 cm distance to the nominal interaction point along the z-axis.

4.3.2 Electrons

Electrons leave a track in the inner tracking system and are stopped in the ECAL, so information from these subdetectors is crucial for their reconstruction [49, 50]. In a simplified view, an electron needs a track matched to an ECAL cluster to be reconstructed. In a more detailed view, electrons in the tracker emit bremsstrahlung which is corrected for with a gaussian sum filter algorithm [51]. The complete reconstruction algorithm incorporates this and groups the energy depositions together by "refining" a supercluster.

Reconstructed electrons have to fulfill certain additional criteria [6, 52]. The pseudorapidity has to be in the range $|\eta| < 2.4$ but not in the transition region between barrel and endcap of the ECAL ($1.4 < |\eta| < 1.6$). Also, a multivariate discriminant for electron identification has to fulfill "tight" working point criteria. Furthermore, electrons have to be isolated in a cone dependent on their transverse momentum (mini isolation) to ensure that they originate from a prompt decay. The cone size in the ϕ-η-plane is defined as

$$R = \frac{10.}{\min\left[\max(50, p_T), 200\right]},$$

so it varies between a size of 0.2 at $p_T < 50\,\text{GeV}$ and 0.05 at $p_T > 200\,\text{GeV}$. For the calculation of the mini isolation, pileup is subtracted using the average energy density ρ and the effective area of the electron's isolation cone. The isolation requirement is for energy depositions in the cone around the electron to not exceed 10 % of its transverse momentum. Additionally, conversion rejection requirements are used. In 2016 data, requirements on the impact parameters, which measure the track's distance to the primary vertex, are also made, because the triggers used in that year do not include these requirements. The transverse impact parameter is required to be smaller than 0.5 mm, while the longitudinal impact parameter is required to be smaller than 1 cm.

4.3.3 Muons

Muons leave a track in the inner tracking system and in the muon system while typically not creating large clusters in the calorimeters. They are reconstructed [32, 53] by a global track fit combining data from both tracking systems. This global fit is only performed if the two independently reconstructed tracks are compatible within three standard deviations.

As the muon chambers only extend over the pseudorapidity range $|\eta| < 2.4$, muons are required in this analysis to be in this range while also excluding $1.4 < |\eta| < 1.6$. This selection is the same as for electrons, ensuring similar kinematics. Additionally medium identification requirements, as they are recommended by the muon Physics Object Group (POG), are imposed on muons. These requirements contain different quantities describing fit quality among other things. Mini isolation requirements of 20 % are imposed on muons. In 2016 data, muons have to fulfill the same impact parameter constraints as electrons.

4.3.4 Jets

Charged hadrons leave tracks in the inner tracking system and energy clusters in the HCAL. As charged hadrons (and photons) carry about 90 % of the average jet energy, it is important that their momentum is precisely measured by the inner tracking system (or the ECAL), which has a significantly better energy resolution than the HCAL. Neutral hadrons, which do not leave a track, but do create a cluster in the HCAL are measured with a lower precision of $120\,\%/\sqrt{E[\mathrm{GeV}]}$. Hadrons are clustered together with the anti-k_T algorithm [54] which is implemented in the FASTJET [55,56] package, using a distance parameter of $R = 0.4$. Charged hadrons not originating from the primary vertex are excluded from clustering. The detector response, which leads to jet energies usually being measured too low, as well as pileup effects are corrected for with so-called type-I jet energy corrections [57]. Type-I corrections consist of several corrections that are performed in a fixed order and reduce influences of pileup and mismeasurements:

1. Pileup corrections are applied based on a simulated QCD sample with and without the incorporation of pileup in the simulation. The differences are parametrized by the transverse jet momentum, jet pseudorapidity, jet area, and offset energy density. These corrections are used for both data and simulation.

2. Jet response corrections are performed on the basis of differences between data and simulation using generator information. For this, QCD dijet events are used. The corrections are parameterized by the jet pseudorapidity and transverse jet momentum. Response corrections are also applied to both data and simulation.

3. Residual corrections correct for remaining differences between simulation and data. These corrections are composed of relative corrections dependent on pseudorapidity and absolute corrections dependent on transverse momentum. The sum of these corrections accounts for dependencies of the jet energy scale and is only applied to data.

Reconstructed jets are required to have a transverse momentum of $p_T > 35\,\mathrm{GeV}$ and to be in the pseudorapidity range $|\eta| < 2.4$. They also have to be more than $\Delta R = 0.4$ away from already reconstructed leptons. Jets from b quarks are identified using the CSV algorithm [58].

4.3.5 Missing Transverse Energy

Before a collision, the transverse momentum of the colliding particles is negligible. Since neutrinos escape the detector undetected they create an imbalance in transverse measurements. This imbalance is quantified by the missing transverse energy (E_T^{miss}) which is defined as the absolute amount of the vectorial sum of the transverse momenta of all particles reconstructed by PF:

$$\vec{p}_T^{\mathrm{miss}} = - \sum_{\text{all objects}} \vec{p}_T \tag{4.1}$$

$$E_T^{\mathrm{miss}} = |\vec{p}_T^{\mathrm{miss}}| \tag{4.2}$$

In the following, $\vec{E}_T^{\mathrm{miss}} = \vec{p}_T^{\mathrm{miss}}$ is used. Besides neutrinos, any stable, electrically neutral particle from non-SM theories could also create missing transverse energy, which is why it is an important quantity to measure when searching for SUSY. Another common cause for missing transverse energy is the mismeasurement of jet energies. This effect leads to an exponentially falling E_T^{miss} spectrum so that processes with neutrino (and possibly neutralino) production are dominant at high values of E_T^{miss}. The type-I jet energy corrections are propagated to E_T^{miss}. In the following, uncorrected missing transverse energy is denoted as $E_T^{\mathrm{miss,uncorr}}$ and missing transverse energy with jet energy corrections applied is denoted as E_T^{miss} or as $E_T^{\mathrm{miss,type\text{-}I}}$ if context is needed.

4.4 Event Selection

The baseline selection of physics objects after reconstruction defines the lepton pair of an event as the two opposite-sign leptons with the highest transverse momenta. The dilepton invariant mass is calculated from the four-momentum the of lepton pair. Additional requirements of the baseline event selection are listed in Table 1.

Table 1: Baseline event selection for events used in the analyses of 2015 and 2016.

Quantity	2015	2016
Leading lepton p_T [GeV]	> 20	> 50
Trailing lepton p_T [GeV]	> 20	> 25
Dileptonic mass $m_{\ell\ell}$ [GeV]	> 20	
ΔR between leptons (dilepton system with Z mass)	> 0.1	
ΔR between leptons (not Z mass)	> 0.3	-
Number of selected jets N_{jets}	≥ 2	

5 Signal Regions

Signal regions are defined to reduce the total number of events in which to search for a specific process, while still retaining as many expected signal events as possible. For the two considered searches for SUSY in 2015 and 2016, different focuses were set, so the signal regions are different.

5.1 Search in 2015

The search for SUSY in 2015 [6] was performed as a follow-up to the results obtained in the 2012 search [5] at 8 TeV in which a 2.6 σ excess over SM expectations was found in the data.

The search is performed in events with same-flavor leptons ($e^{\pm}e^{\mp} + \mu^{\pm}\mu^{\mp}$). At least two jets and a missing transverse energy greater than 150 GeV or at least three jets and a missing transverse energy greater than 100 GeV are required for all signal regions. The signal regions are categorized into events, where both leptons have $|\eta| < 1.4$ (central) and where at least one lepton has $|\eta| > 1.6$ (forward). For some uses, the central and forward region are shown combined. This combined region is labeled inclusive. An additional division of the signal regions is done in the dileptonic mass. The five mass regions are summarized in Table 2 along with all other signal region requirements.

5.2 Search in 2016

The search of 2016 [52] is performed as a follow-up search to an excess over SM expectation in dileptonic same-flavor events found by ATLAS in 2012 [7] and 2015 [8]. The excess was found for dilepton masses compatible with the Z boson mass. Only one search region, which is similar to the region in which ATLAS found the excess, is used.

The search is based on the JZB method (6.2.1), thus the signal region has a requirement of JZB $>$ 225 GeV. Other requirements include the hadronic activity plus transverse momenta of both leptons and the angle between the two leading jets and missing transverse energy. The signal region definition is summarized in Table 3.

The first requirement on the angles between $\vec{E}_T^{\text{miss}}$ and the leading jets was used by

Table 2: Signal region definitions in the 2015 search

Base requirement	
Same-flavor leptons ($e^{\pm}e^{\mp} + \mu^{\pm}\mu^{\mp}$)	
$E_T^{\text{miss}} > 100\,\text{GeV} \wedge N_{\text{jets}} \geq 3 \vee$	
$E_T^{\text{miss}} > 150\,\text{GeV} \wedge N_{\text{jets}} \geq 2$	
Mass regions	
Low mass	$20 < m_{\ell\ell} < 70\,\text{GeV}$
Below Z	$70 < m_{\ell\ell} < 81\,\text{GeV}$
On Z	$81 < m_{\ell\ell} < 101\,\text{GeV}$
Above Z	$101 < m_{\ell\ell} < 120\,\text{GeV}$
High mass	$m_{\ell\ell} > 120\,\text{GeV}$
Pseudorapidity regions	
Central	Both leptons $\lvert\eta\rvert < 1.4$
Forward	At least one lepton $\lvert\eta\rvert > 1.6$

Table 3: Signal region definition for the 2016 search

Same-flavor leptons ($e^{\pm}e^{\mp} + \mu^{\pm}\mu^{\mp}$)	
JZB	$> 225\,\text{GeV}$
N_{Jets}	≥ 2
$m_{\ell\ell}$	$> 81\,\text{GeV}$
$m_{\ell\ell}$	$< 101\,\text{GeV}$
$H_T + p_T^{\ell_1} + p_T^{\ell_2}$	$> 600\,\text{GeV}$
$\lvert\Delta\phi(\vec{E}_T^{\text{miss}}, j_{1/2})\rvert$	> 0.4
$\lvert\Delta\phi(\vec{E}_T^{\text{miss}}, j_{1/2}) - \pi\rvert$	> 0.4

the search employed by ATLAS to suppress the Drell-Yan background. The second requirement was added to the search region especially for this search in order to be able to use the JZB method (Sec. 6.2.1).

5.3 Standard Model Backgrounds

The definition of the signal regions always includes two opposite-sign same-flavor leptons, multiple jets and missing transverse energy (or an equivalent such as JZB). This leads to different SM processes with multiple jet production contributing to the signal regions in a significant way. The most relevant process is the dileptonic $t\bar{t}$ process, which produces multiple jets as well as genuine missing transverse energy from its neutrinos. An example $t\bar{t}$ Feynman diagram is shown in Fig. 7.

Another important background is the Drell-Yan (DY) process. Jets in this process come from intial or final state radiation, therefore most events from this process have a low jet multiplicity. Neutrinos are only produced in the leptonic decay of DY $\rightarrow \tau\tau$. The other decays produce no genuine missing transverse energy. Therefore, missing transverse energy in the DY process mainly originates from mismeasurements of the jet

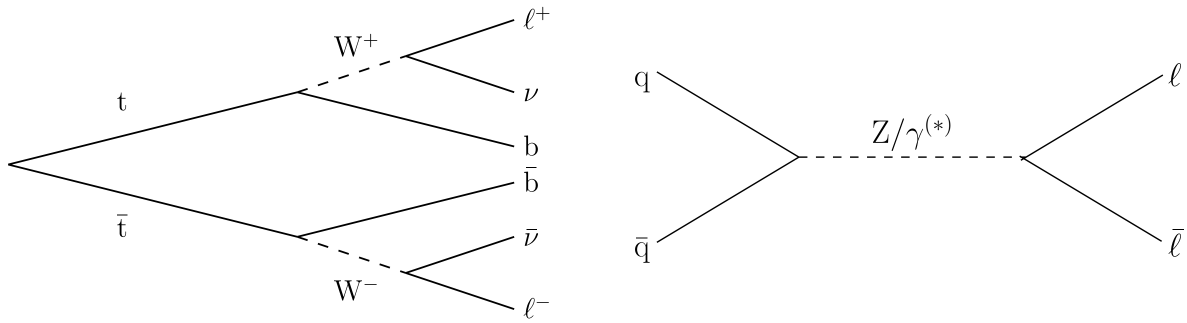

Figure 7: Feynman diagrams of the dileptonic $t\bar{t}$ decay (left) and the Drell-Yan process (right)

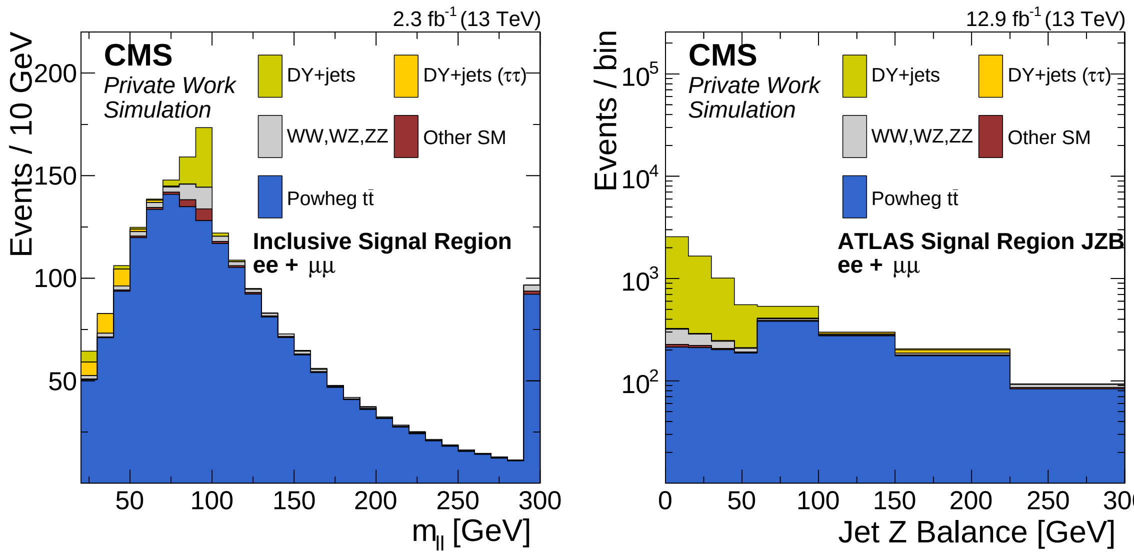

Figure 8: Background composition in the signal regions of the 2015 search (left, inclusive selection) and the 2016 search (right, without JZB > 225 GeV requirement)

energies, resulting in a steeply falling missing transverse energy distribution. Because of the high cross section of this process, it is an important background and is most relevant in search regions with dileptonic masses compatible with the Z boson mass (with exception of DY $\rightarrow \tau\tau$). The Feynman diagram of this process without any jet production is shown in Fig. 7.

As can be seen in Fig. 8, several smaller background processes contribute to the signal regions as well. Most of these backgrounds are similar to the already mentioned backgrounds. It should be noted, that the $t\bar{t}$ simulation is not very accurate as it tends to simulate too high jet multiplicities, significantly overestimating the $t\bar{t}$ contribution to the signal region.

6 Background Estimation

The background estimation mainly relies on data-driven methods. The SM background processes can be divided into three classes for which different estimation methods are used.

6.1 Flavor-Symmetric Backgrounds

Backgrounds that produce the same number of same-flavor (SF) and opposite-flavor (OF) events are called flavor symmetric (FS). This includes the dileptonic $t\bar{t}$ process, DY $\rightarrow \tau\tau$ and certain WW and WZ decays. All processes produce genuine missing transverse energy through neutrinos and make up the biggest component of the background.

As the same number of SF and OF events are produced ($N_{OF} = 2N_{\mathrm{ee}} = 2N_{\mu\mu} = N_{SF}$) and most other SM backgrounds as well as the SUSY signal exclusively produce SF dileptons, the OF sample ($e\mu$) can be used as a control sample to estimate the contribution from FS background processes in the signal region. Since SF and OF events are selected with slightly different trigger, reconstruction and selection efficiencies, a scale factor $\mathrm{R_{SF/OF}}$ is used to extrapolate from the OF sample to the SF sample. This factor is determined in two different and independent ways, a direct measurement and a factorization approach.

The direct measurement of $\mathrm{R_{SF/OF}}$ is performed in a control region (Table 4), which is similar but orthogonal to the signal region used in the search performed in 2015. It is also orthogonal to the signal region used for the search in 2016. In this region, $\mathrm{R_{SF/OF}}$ is obtained by calculating the ratio of the numbers of SF and OF events.

Table 4: Definition of the control region for the direct measurement of $\mathrm{R_{SF/OF}}$

N_{Jets}	$= 2$
E_T^{miss}	$> 100\,\mathrm{GeV}$
E_T^{miss}	$< 150\,\mathrm{GeV}$
Divided into central and forward	

The factorization approach is realized by taking trigger efficiencies as well as selection efficiencies into account. The first important factor for this method is the lepton efficiency ratio $r_{\mu e}$ which is calculated in a Drell-Yan enriched region characterized in Table 5. Again, the region is divided intro central and forward.

The reconstruction efficiency ratio is thus defined as

$$r_{\mu\mathrm{e}} = \frac{\epsilon_\mu^{\mathrm{reco}}}{\epsilon_{\mathrm{e}}^{\mathrm{reco}}} = \sqrt{\frac{N_{\mu\mu}}{N_{\mathrm{ee}}}}. \tag{6.1}$$

Here and in the next steps, it is assumed that $\epsilon_\ell = \sqrt{\epsilon_{\ell\ell}}$. Using the $r_{\mu\mathrm{e}}$ factor, a

Table 5: Definition of the Drell-Yan enriched region

N_{Jets}	≥ 2
E_T^{miss}	$< 50\,\text{GeV}$
$m_{\ell\ell}$	$> 81\,\text{GeV}$
$m_{\ell\ell}$	$< 101\,\text{GeV}$
Divided into central and forward	

first estimation of the number of SF $\text{t}\bar{\text{t}}$ events can be made (here, $r^*_{\mu\text{e}}$ is the lepton reconstruction efficiency ratio):

$$N^*_{\text{ee}} = r^{-1*}_{\mu\text{e}} \cdot N_{\text{e}\mu} \cdot 0.5 \tag{6.2}$$

$$N^*_{\mu\mu} = r^*_{\mu\text{e}} \cdot N_{\text{e}\mu} \cdot 0.5 \tag{6.3}$$

$$N^*_{SF} = (r^{-1*}_{\mu\text{e}} + r^*_{\mu\text{e}}) \cdot N_{\text{e}\mu} \cdot 0.5 \tag{6.4}$$

(6.5)

In this estimation, trigger efficiencies are not yet considered. To account for different trigger efficiencies between electrons and muons, trigger efficiencies for each sample are calculated. Trigger efficiencies are measured using an uncorrelated "baseline" trigger, calculating the ratio between events that pass both the considered trigger and the baseline trigger and events that pass the baseline trigger:

$$\epsilon^{\text{trig}}_{\ell\ell} = \frac{\#(\text{Lepton trigger} \wedge \text{Baseline trigger})}{\#(\text{Baseline trigger})} \tag{6.6}$$

The triggers used here as baseline triggers are based on hadronic activity H_T and are listed in Appendix A. The trigger efficiencies in the dataset of 2015 range from 90 % to 96 %. In the dataset of 2016, the trigger efficiency for eμ events dropped to 88 %. Using the dilepton trigger efficiencies, the lepton reconstruction efficiency ratio is defined as

$$r_{\mu\text{e}} = \sqrt{\frac{\epsilon^{\text{trig}}_{\mu\mu}}{\epsilon^{\text{trig}}_{\text{ee}}} r^*_{\mu\text{e}}} \tag{6.7}$$

$$\text{and } R_T = \frac{\sqrt{\epsilon^{\text{trig}}_{\mu\mu}\epsilon^{\text{trig}}_{\text{ee}}}}{\epsilon^{\text{trig}}_{\text{e}\mu}}. \tag{6.8}$$

This definition of $r_{\mu\text{e}}$ is directly measured by taking the ratio of the numbers of ee and $\mu\mu$ events in the Drell-Yan enriched region. Therefore, the number of same-flavor events from flavor-symmetric backgrounds can be estimated as

$$N_{SF} = 0.5 \cdot R_T \times (r^{-1}_{\mu\text{e}} + r_{\mu\text{e}}) \cdot N_{\text{e}\mu} = \text{R}_{\text{SF/OF}} \cdot N_{\text{e}\mu}. \tag{6.9}$$

Dependencies of $r_{\mu\text{e}}$ are accounted for by applying a 10 %(20 %) uncertainty in the central (forward) region, which is then propagated to $R_{SF/OF}$. Because of the way that $r_{\mu e}$ contributes to $R_{SF/OF}$, the resulting systematic uncertainties on the final prediction are significantly smaller. Uncertainties on the trigger efficiencies of about about 5 % are additional systematic uncertainty sources. When directly measuring $R_{SF/OF}$, the uncertainty on a transfer factor between the control and signal region determined on simulation is used to determine the systematic uncertainty.

The $R_{SF/OF}$ method is a well established and robust method for a data-driven estimation of the SF contribution of flavor-symmetric processes and performs well in closure tests on simulated $t\bar{t}$ events. As no significant discrepancies between estimation and observation are found, no additional systematic uncertainty is applied. The results from factorization and direct measurement are compatible within their uncertainties, therefore they are combined with a weighted average. Because of the large dataset, the weighted average was dominated by the direct measurement of $R_{SF/OF}$ in 2016. The resulting values for the data taken in 2015 and 2016 are listed in Table 6.

Table 6: Weighted average of $R_{SF/OF}$ in different kinematic regions for 2015 and 2016. For 2016, only the inclusive result is given.

	2015		2016
	Central	Forward	Inclusive
Data	1.03 ± 0.05	1.08 ± 0.07	1.091 ± 0.023
MC	1.04 ± 0.03	1.07 ± 0.04	1.101 ± 0.003

6.2 Drell-Yan like processes

Processes that produce opposite-sign same-flavor dilepton pairs and no genuine missing transverse energy are the second most important background for the signal regions. These processes include most prominently the Drell-Yan process, but also certain ZZ and WZ processes where one boson produces a dilepton pair and the other one decays into quarks. These backgrounds mostly populate the mass region around the Z boson mass and the missing transverse energy in these events originates from the mismeasurement of jets. These processes are grouped under the name Z+jets.

Two independent methods of estimating these backgrounds are employed. Both methods are based on estimating the number of Z+jets events on the Z peak and, if necessary, extrapolating the result to other mass regions with a scale factor $R_{\mathrm{out/in}}$. This scale factor is determined in the Drell-Yan enriched region by calculating the ratio of the number of events in a selected mass region and the Z peak ($81 < m_{\ell\ell} < 101$ GeV). To remove the influence of any flavor-symmetric backgrounds, the scale factor $\mathrm{R_{SF/OF}}$ is used:

$$R_{\mathrm{out/in}} = \frac{N_{SF}^{\text{off-Z}} - \mathrm{R_{SF/OF}} \cdot N_{OF}^{\text{off-Z}}}{N_{SF}^{\text{on-Z}} - \mathrm{R_{SF/OF}} \cdot N_{OF}^{\text{on-Z}}} \tag{6.10}$$

The determination of $R_{\mathrm{out/in}}$ in the Drell-Yan enriched region on the dataset of 2015 is shown in Fig. 9.

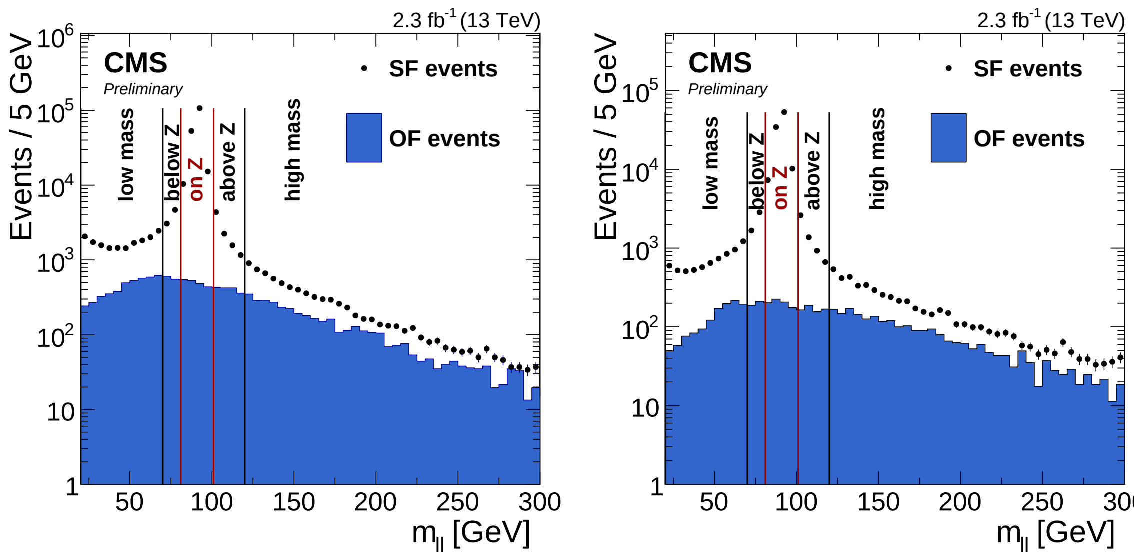

Figure 9: Determination of the $R_{\mathrm{out/in}}$ scale factor in the central (left) and forward (right) region.

Differences in the mass distribution between the Drell-Yan enriched region and the signal region as well as dependencies of $R_{\mathrm{out/in}}$ are accounted for by applying a 25 % systematic uncertainty on the extrapolation, which covers these differences. This extrapolation is only necessary for the 2015 analysis as the signal region for the search in 2016 is defined on the Z mass peak. The determined values of $R_{\text{out/in}}$ are listed in Table 7. Systematic uncertainties are included in the uncertainties of the given values.

Table 7: Determined values of $R_{\text{out/in}}$

	Low Mass	Below Z	Above Z	High Mass
Central	0.073 ± 0.018	0.043 ± 0.011	0.037 ± 0.009	0.023 ± 0.005
Forward	0.056 ± 0.014	0.047 ± 0.012	0.041 ± 0.010	0.030 ± 0.007

6.2.1 The Jet-Z Balance method

The Jet-Z Balance (JZB) method is a method for the estimation of the Z+jets background in events with multiple jets. It was employed in past analyses including the search for SUSY in dileptonic events in 2012 [5], but was not used for the follow-up analysis in 2015. The aim of this thesis is to reutilize the JZB method by providing an independent cross check for the Drell-Yan background estimation of the 2015 analysis [6] and to apply the JZB method to a dedicated search in the dataset of 2016.

The JZB method uses the event kinematics of the Drell-Yan process and the fact that the process does not produce genuine missing transverse energy. It is based on the JZB variable which is defined as the difference between hadronic recoil and the transverse momentum of the Z boson of an event:

$$\text{JZB} = \left| \sum_{\text{jets}} \vec{p}_T \right| - \left| \vec{p}_T^{\ell\ell} \right| \tag{6.11}$$

As Z+jets events only contain leptons and jets, JZB can be rewritten using $\vec{E}_T^{\text{miss}} = -\sum_{\text{jets}} \vec{p}_T - \vec{p}_T^{\ell\ell}$:

$$\text{JZB} = \left| \vec{E}_T^{\text{miss}} + \vec{p}_T^{\ell\ell} \right| - \left| \vec{p}_T^{\ell\ell} \right| \tag{6.12}$$

This gives the advantage of including all particles identified by the Particle Flow algorithm, also considering jets that are not reconstructed because of low transverse momentum or failing other reconstruction criteria.

For Z+jets events with one jet, this jet and the dilepton system recoil against each other. Missing transverse energy in Z+jets processes mainly results from the mismeasurement of jet energies, while the dilepton system is generally well measured and contributes very little.

JZB can be interpreted as an indicator of the origin of missing transverse energy in the one-jet case, namely if the jet energy was measured too low (resulting in negative values of JZB) or too high (resulting in positive values of JZB). The one-jet scenario is shown in Fig. 10. Due to energy losses, measuring the jet energy too low is more

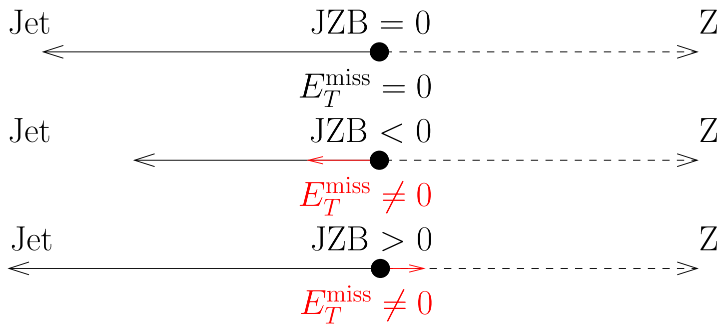

Figure 10: Sketches of Z+jets events with different scenarios for JZB and E_T^{miss} in the case of one jet. The shown momenta of the physical objects are not the actual momenta but the momenta measured by the detector.

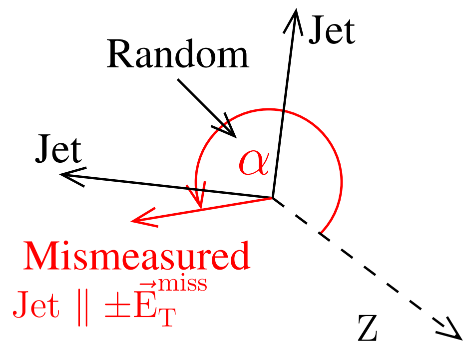

Figure 11: Sketch of the angular randomization of the mismeasured jet that contributes to E_T^{miss} in a three-jet Z+jets event.

probable than measuring it too high, thus the JZB distribution for one jet is skewed towards negative values.

For events with higher jet multiplicities, the kinematics get more complicated. Multiple jets can contribute to the missing transverse energy through their mismeasurements, however the mismeasurements can also cancel each other out. Already for three jets, the most probable configuration is the two leading jets pointing back-to-back while the third jet has a random angular direction with regard to the Z boson [59]. A possible configuration of three jets is shown in Fig. 11.

Because of the angular randomization of the missing transverse energy, the JZB distribution is symmetric around 0. This is best visible for high jet multiplicities, where the distribution approaches a Gaussian shape, but for events with two jets, the JZB distribution is already only asymmetric in the positive and negative tails.

Flavor-symmetric backgrounds produce genuine E_T^{miss} through neutrinos. Therefore, the JZB distribution of these processes is biased towards positive values. The JZB distribution of these backgrounds is also symmetric between SF and OF events.

The signal model has a more complex event structure as the $\tilde{\chi}_1^0$ can be produced together with one of the leptons while the other lepton is produced in an earlier step. Because of the unknown SUSY particle masses, it is not clear whether the first lepton would be boosted in the same direction as the other lepton and the $\tilde{\chi}_1^0$ or recoil against them. There is also a second neutralino in each event. Because of the genuine missing transverse energy that is produced, the signal model process is expected to produce a large fraction of events with positive values of JZB. A comparison of the expected JZB distributions of the Drell-Yan process, the $\mathrm{t\bar{t}}$ process and an example signal point is shown in Fig. 12.

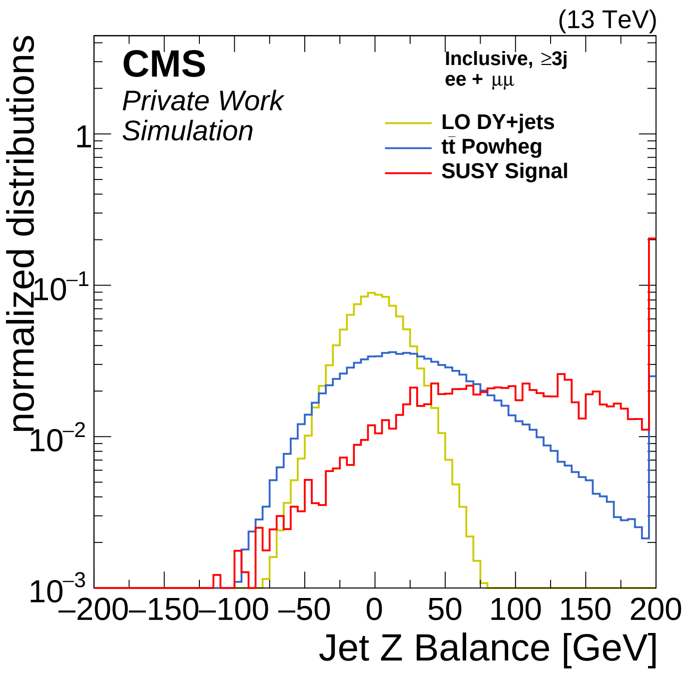

Figure 12: Comparison of the normalized JZB spectra of simulated Drell-Yan, $\mathrm{t\bar{t}}$ and signal samples. The signal sample parameters are $m_{\tilde{\mathrm{b}}} = 450\,\mathrm{GeV}$ and $m_{\tilde{\chi}_2^0} = 150\,\mathrm{GeV}$. Three or more jets are required.

For the application of the JZB method, it is assumed that the majority of signal events populate the region of JZB > 0, while at JZB < 0 the signal is depleted. Therefore, JZB < 0 is defined as a control region and the symmetry of the JZB spectrum around zero for Z+jets events is used to predict the number of Z+jets events with JZB > 0. In events with two or more jets, the number of Z+jets events is estimated as

$$N_{SF}^{\mathrm{Z+jets}}(\mathrm{JZB} > X) = N_{SF}^{\mathrm{Z+jets}}(\mathrm{JZB} < -X), \tag{6.13}$$

where X is an arbitrary positive threshold. As some events from flavor-symmetric SM processes have negative values of JZB, this formula has to be modified to be applicable on data. To remove the contribution by flavor-symmetric processes, the $\mathrm{R_{SF/OF}}$ method is used:

$$N_{SF}^{\mathrm{Z+jets}}(\mathrm{JZB} > X) = N_{SF}(\mathrm{JZB} < -X) - \mathrm{R_{SF/OF}} \cdot N_{OF}(\mathrm{JZB} < -X) \tag{6.14}$$

Using this formula, the number of Z+jets events in the signal region defined for the search in 2016 can be estimated.

Prediction of the E_T^{miss} Spectrum

As the signal region for the search performed in 2015 is not defined with JZB, but with an E_T^{miss} threshold, the JZB method cannot be directly applied. However, as JZB is defined through E_T^{miss}, the two observables are correlated. From the definition of JZB, it is given that $|\text{JZB}| < E_T^{\text{miss}}$. As positive and negative values of JZB in Z+jets events arise from the angular randomization of $\vec{E}_T^{\text{miss}}$ with respect to the Z boson, the E_T^{miss} spectra of JZB < 0 and JZB > 0 have to be identical for the JZB spectrum to be symmetric around 0. Therefore, the E_T^{miss} spectrum of Z+jets can be estimated as follows:

$$N_{SF}^{\text{Z+jets}}(\text{JZB} > 0, E_T^{\text{miss}} > X) = N_{SF}(\text{JZB} < 0, E_T^{\text{miss}} > X) \\ -\text{R}_{\text{SF/OF}} \cdot N_{OF}(\text{JZB} < 0, E_T^{\text{miss}} > X) \quad (6.15)$$

and thus

$$N_{SF}^{\text{Z+jets}}(E_T^{\text{miss}} > X) = 2 \cdot [N_{SF}(\text{JZB} < 0, E_T^{\text{miss}} > X) \\ -\text{R}_{\text{SF/OF}} \cdot N_{OF}(\text{JZB} < 0, E_T^{\text{miss}} > X)] \quad (6.16)$$

Using Eq. (6.16), one can integrate the JZB method into searches that use signal regions which are not defined by a JZB threshold, but by a E_T^{miss} requirement.

Because of effects such as pileup and the detector response to jets, the measured JZB distribution is not symmetric around zero. These effects are compensated by applying corrections to the JZB variable in several steps. For each step, the corrections derived from the previous steps are applied. The corrections are determined on data and simulation and are applied event-by-event. The event selection used for the determination of the corrections is different between the analyses of 2015 and 2016. The selection for the search in data taken in 2015 is shown in Table 8, the selection for the search in data taken in 2016 in shown in Table 9.

The event selection used is similar to the signal region definition of each search, omitting only the requirements on E_T^{miss} or JZB. The corrections are also separately calculated in different regions which are kinematically different. For the 2015 search this separation is done in jet multiplicity and lepton pseudorapidity. As the selection constraints for the 2016 search are much tighter, the separation into different jet multiplicities is not performed in order to retain a high enough number of events in each selection. In the 2016 search, the first two correction steps were also interchanged in order to achieve the best possible closure. Below, only the determination of cor-

Table 8: Event selection for calculating the corrections to JZB for the search in the dataset of 2015

Base requirement	
Same-flavor leptons	($e^{\pm}e^{\mp} + \mu^{\pm}\mu^{\mp}$)
On Z	$81 < m_{\ell\ell} < 101\,\mathrm{GeV}$
Pseudorapidity regions	
Central	Both leptons $\lvert\eta\rvert < 1.4$
Forward	At least one lepton $\lvert\eta\rvert > 1.6$
Jet multiplicity	
Two jets	$N_{\mathrm{Jets}} = 2$
Three or more jets	$N_{\mathrm{Jets}} \geq 3$

Table 9: Event selection for calculating the corrections to JZB for the search in the dataset of 2016

Base requirement	
Same-flavor leptons	($e^{\pm}e^{\mp} + \mu^{\pm}\mu^{\mp}$)
N_{Jets}	≥ 2
On Z	$81 < m_{\ell\ell} < 101\,\mathrm{GeV}$
$H_T + p_T^{\ell_1} + p_T^{\ell_2}$	$> 600\,\mathrm{GeV}$
$\lvert\Delta\phi(\vec{E}_T^{\mathrm{miss}}, j_{1/2})\rvert$	> 0.4
$\lvert\Delta\phi(\vec{E}_T^{\mathrm{miss}}, j_{1/2}) - \pi\rvert$	> 0.4
Pseudorapidity regions	
Central	Both leptons $\lvert\eta\rvert < 1.4$
Forward	At least one lepton $\lvert\eta\rvert > 1.6$

rections for the dataset of 2015 is shown as the procedure for the dataset of 2016 is very similar. For all corrections, opposite-flavor subtractions is performed to remove flavor-symmetric backgrounds.

In previous searches, uncorrected E_T^{miss} was used. To examine the influence of using $E_T^{\mathrm{miss,type\text{-}I}}$ instead of $E_T^{\mathrm{miss,uncorr}}$ on the JZB method, the corrections are calculated for both definitions of missing transverse energy.

Response Corrections

The first correction step is performed to correct for the jet response being not equal to unity. If the jet response (R) is different from unity, the hadronic recoil in Z+jets events is either measured too high ($R > 1$) or too low ($R < 1$). As the hadronic recoil is proportional to the transverse momentum of the Z boson, this results in a dependence of the JZB peak on the transverse momentum of the Z boson. In principle, this should already be corrected by type-I corrections that correct for the jet response, however for the specific dataset and selection, there might still be small deviations from $R = 1$.

The JZB response is defined as

$$R_{\mathrm{JZB}} = \frac{|\vec{E}_T^{\mathrm{miss}} + \vec{p}_T^{\ell\ell}|}{|\vec{p}_T^{\ell\ell}|}. \tag{6.17}$$

The JZB response distribution is plotted against the transverse momentum of the lepton pair in Fig. 13. The mean value of R_{JZB} is determined by a constant line fit between $100 < p_T^{\ell\ell} < 400\,\mathrm{GeV}$.

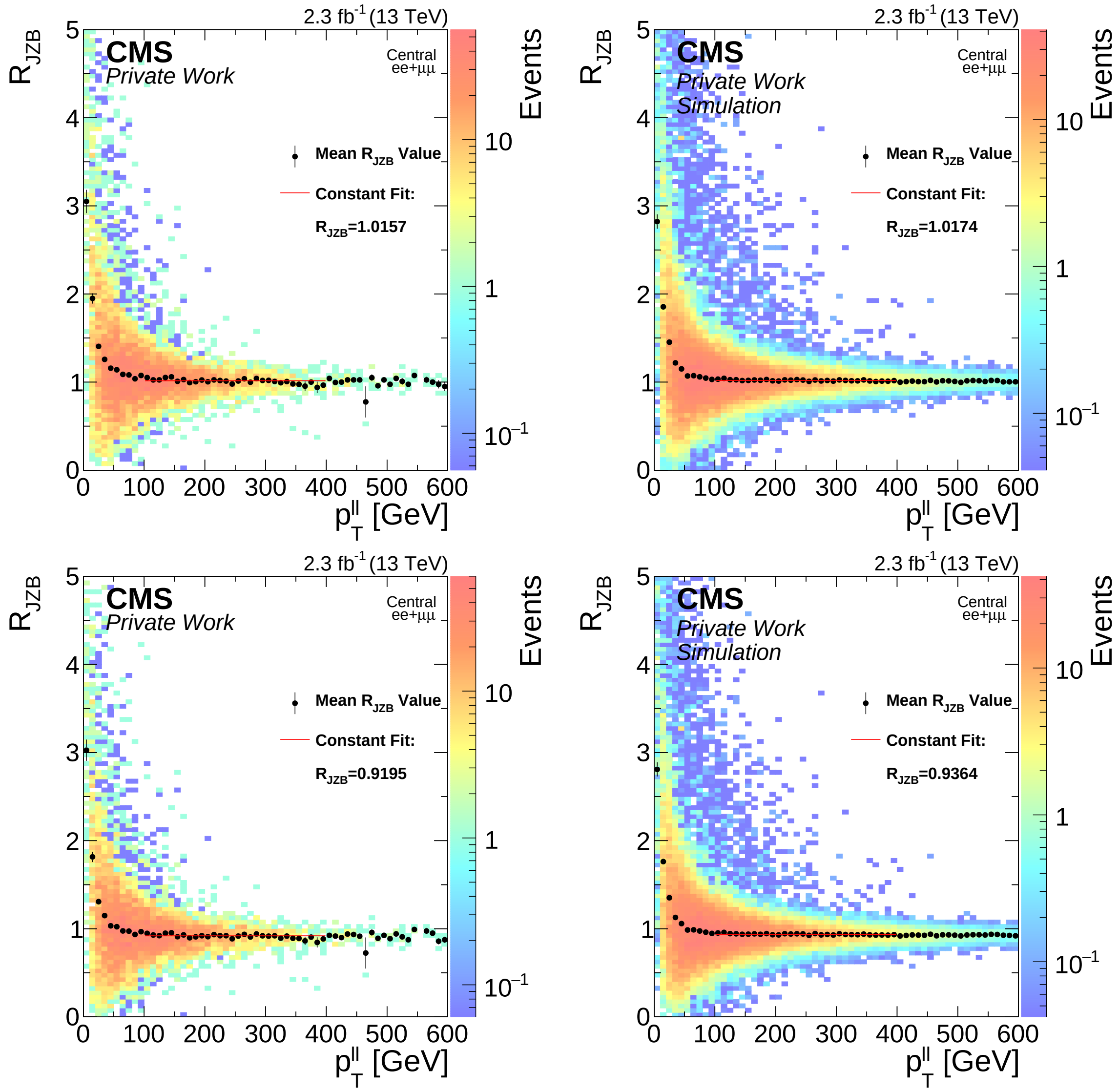

Figure 13: Dependence of JZB response on the dilepton transverse momentum. The chosen selection is central with three or more jets, shown are the distributions in data (left) and simulation (right), as well as using type-I corrected missing transverse energy (top) and uncorrected missing transverse energy (bottom).

Using $E_T^{\mathrm{miss,type\text{-}I}}$, the response deviates upwards from unity by about $1-3\,\%$ in both data and simulation. If the distributions are considered using $E_T^{\mathrm{miss,uncorr}}$, the deviations in data and simulation are different from each other and are smaller than unity by up to 8.5 %. An explanation for differences between data and simulation using uncorrected missing transverse energy is that type-I corrections are tuned by comparing data and simulation, trying to reduce detector effects. To apply response corrections, the difference of the fitted response from unity, defined as $\alpha = R_{\mathrm{JZB}} - 1$, is multiplied by the dilepton transverse momentum and added to JZB for each event:

$$\mathrm{JZB} = \mathrm{JZB}_{\mathrm{raw}} + \alpha \cdot p_T^{\ell\ell} \tag{6.18}$$

Here, $\mathrm{JZB}_{\mathrm{raw}}$ denotes JZB without any corrections applied. Applying the response corrections restores the invariance of the JZB peak for high values of $p_T^{\ell\ell}$ as can be seen for $E_T^{\mathrm{miss,uncorr}}$ in Fig. 14. The determined values of α are listed in Table 10.

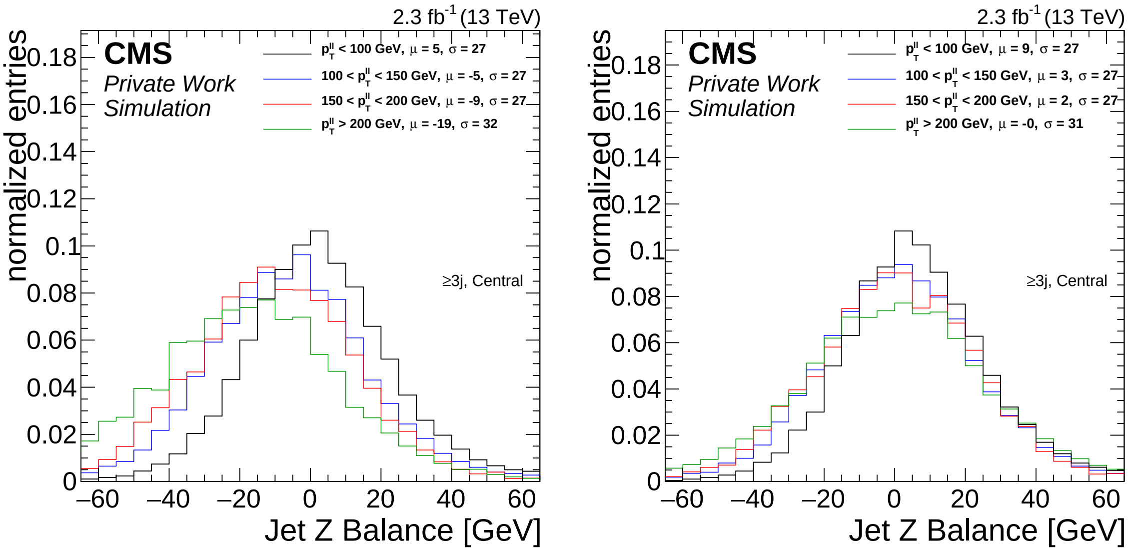

Figure 14: Peak position in dependence of the dilepton transverse momentum of JZB without (left) and with (right) applied response corrections. Shown are simulated events in the central region; uncorrected missing transverse energy is used.

Table 10: Response corrections determined on data and simulation using type-I corrected and uncorrected missing transverse energy. Note, that the corrections extracted from the dataset of 2016 are expected to strongly differ from the corrections determined on the dataset of 2015 as the response corrections were applied as the second corrections in that analysis. In that case, the JZB response recieved a correction term $\beta \cdot N_{\text{vertices}}/p_T^{\ell\ell}$ for each event.

Data

α	2015				2016	
	$E_T^{\text{miss,type-I}}$		$E_T^{\text{miss,uncorr}}$		$E_T^{\text{miss,type-I}}$	
	Central	Forward	Central	Forward	Central	Forward
$N_{\text{Jets}} = 2$	−0.017	−0.021	0.083	0.079	0.010	0.002
$N_{\text{Jets}} \geq 3$	−0.016	−0.010	0.081	0.085		

Simulation

α	2015				2016	
	$E_T^{\text{miss,type-I}}$		$E_T^{\text{miss,uncorr}}$		$E_T^{\text{miss,type-I}}$	
	Central	Forward	Central	Forward	Central	Forward
$N_{\text{Jets}} = 2$	−0.023	−0.027	0.059	0.057	−0.005	−0.006
$N_{\text{Jets}} \geq 3$	−0.017	−0.021	0.064	0.061		

Pileup Peak Corrections

Pileup lowers the energy resolution and thus leads to higher values of missing transverse energy. It can be observed that with an increasing number of interaction vertices per event, the JZB peak shifts towards higher values. To remove the pileup dependence of the JZB peak, the JZB distribution is plotted against the number of reconstructed vertices and the JZB peak position for a certain vertex multiplicity is extracted by fitting a Gaussian function to the JZB distribution between −50 and 50 GeV. The fitted peak position is plotted against the number of vertices and a linear fit to the peak position is performed to obtain the slope (Fig. 15).

In data, all regions show similar dependencies around 0.16 GeV/N_{vertices}, with slightly higher values for uncorrected missing transverse energy. However, for high numbers of vertices, some plots show non-linear behaviour, although with high uncertainties on the outlying points due to low statistical significance. Given that there is no compelling reason to assume a linear dependency of the JZB peak position on pileup, the linear fits describe the data well. In simulation, the slopes extracted from the different regions strongly deviate between each other, ranging from 0.08 to 0.20 GeV/N_{vertices}. This is probably due to an imperfect description of pileup in the simulated samples. The dependencies in the dataset of 2016 and simulation are significantly lower, which is expected due to the requirement of a high hadronic activity supressing the influence of pileup jets. The fitted slopes β are multiplied with the number of vertices and subtracted from JZB to remove the pileup dependency of the JZB peak.

$$\text{JZB} = \text{JZB}_{\text{raw}} + \alpha \cdot p_T^{\ell\ell} - \beta \cdot N_{\text{vertices}} \tag{6.19}$$

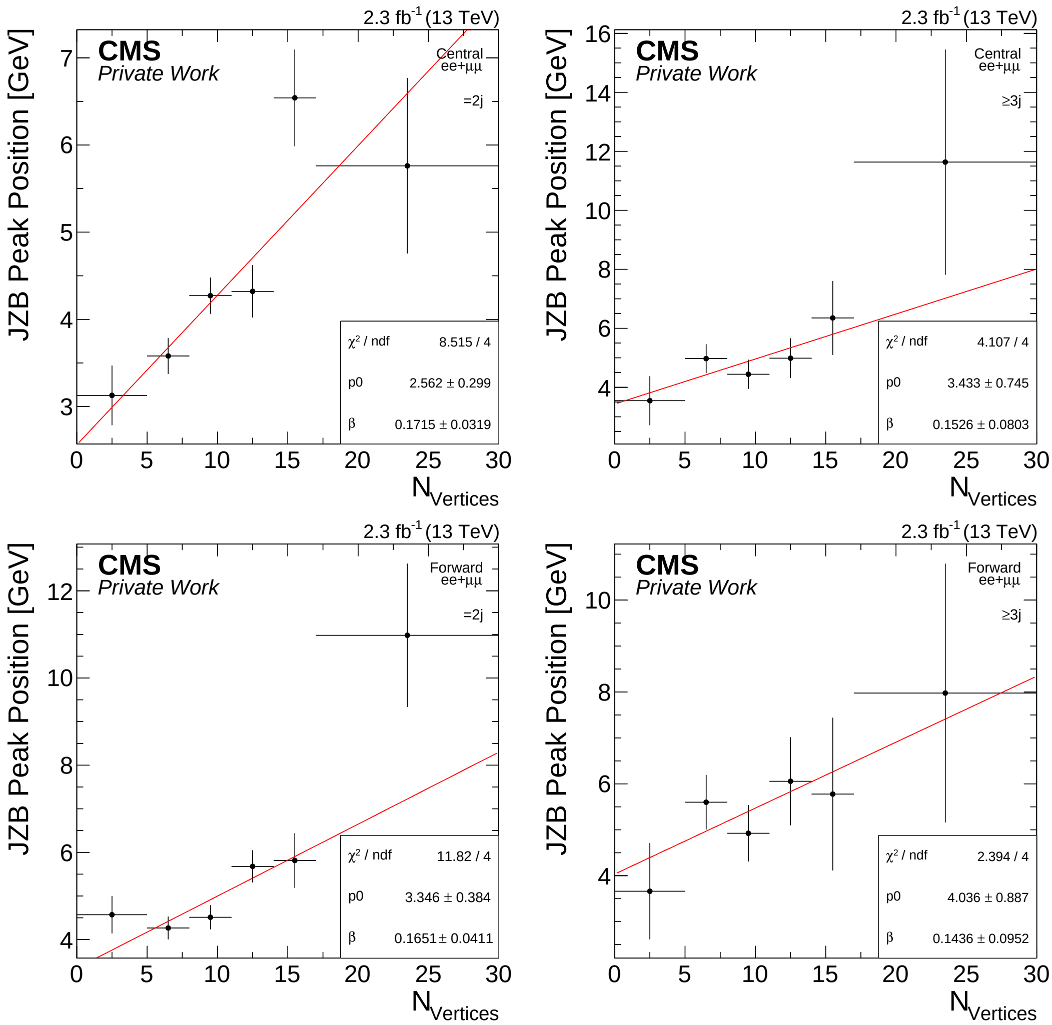

Figure 15: Dependency of the JZB peak position on the vertex multiplicity. Shown are data with two (left) or three or more (right) jets in the central (top) and forward (bottom) regions. Type-I corrected missing transverse energy is used.

A summary of the pileup corrections is given in Table 11.

Table 11: Pileup corrections for data and simulation.

Data						
β [GeV]/N_{vertices}	2015				2016	
	$E_T^{\text{miss,type-I}}$		$E_T^{\text{miss,uncorr}}$		$E_T^{\text{miss,type-I}}$	
	Central	Forward	Central	Forward	Central	Forward
$N_{\text{Jets}} = 2$	0.17	0.17	0.19	0.20	0.10	0.014
$N_{\text{Jets}} \geq 3$	0.15	0.14	0.16	0.15		

Simulation						
β [GeV]/N_{vertices}	2015				2016	
	$E_T^{\text{miss,type-I}}$		$E_T^{\text{miss,uncorr}}$		$E_T^{\text{miss,type-I}}$	
	Central	Forward	Central	Forward	Central	Forward
$N_{\text{Jets}} = 2$	0.16	0.20	0.16	0.21	0.033	0.005
$N_{\text{Jets}} \geq 3$	0.08	0.17	0.09	0.20		

Peak Corrections

As a last step, the peak position of the JZB distribution is centered to zero. This is done by fitting a Gaussian distribution to the JZB spectrum and shifting all values by the fitted mean value μ. This correction factor is strongly dependent on the previous corrections, thus different values are expected for uncorrected and type-I corrected E_T^{miss}. Fit results using type-I corrected E_T^{miss} are shown in Fig. 16.

In both data and simulation, the JZB distributions are more peaked in their maximum than a Gaussian function but are described well by the fit outside the peak region. The fit results vary between 1.6 and 4.1 GeV in data and between 1.5 and 2.6 GeV in simulation. In the dataset of 2016, the peak corrections are consistently above 4 GeV. The peak corrections are summarized in Table 12.

Table 12: Peak corrections for data and simulation.

Data						
μ [GeV]	2015				2016	
	$E_T^{\text{miss,type-I}}$		$E_T^{\text{miss,uncorr}}$		$E_T^{\text{miss,type-I}}$	
	Central	Forward	Central	Forward	Central	Forward
$N_{\text{Jets}} = 2$	2.3	3.1	1.6	2.1	4.6	4.2
$N_{\text{Jets}} \geq 3$	3.2	4.1	2.5	3.2		

Simulation						
μ [GeV]	2015				2016	
	$E_T^{\text{miss,type-I}}$		$E_T^{\text{miss,uncorr}}$		$E_T^{\text{miss,type-I}}$	
	Central	Forward	Central	Forward	Central	Forward
$N_{\text{Jets}} = 2$	1.7	1.5	1.6	1.4	2.1	2.4
$N_{\text{Jets}} \geq 3$	2.6	2.1	2.3	1.7		

To include the peak corrections, JZB is defined as

$$\text{JZB} = \text{JZB}_{\text{raw}} + \alpha \cdot p_T^{\ell\ell} - \beta \cdot N_{\text{vertices}} - \mu. \tag{6.20}$$

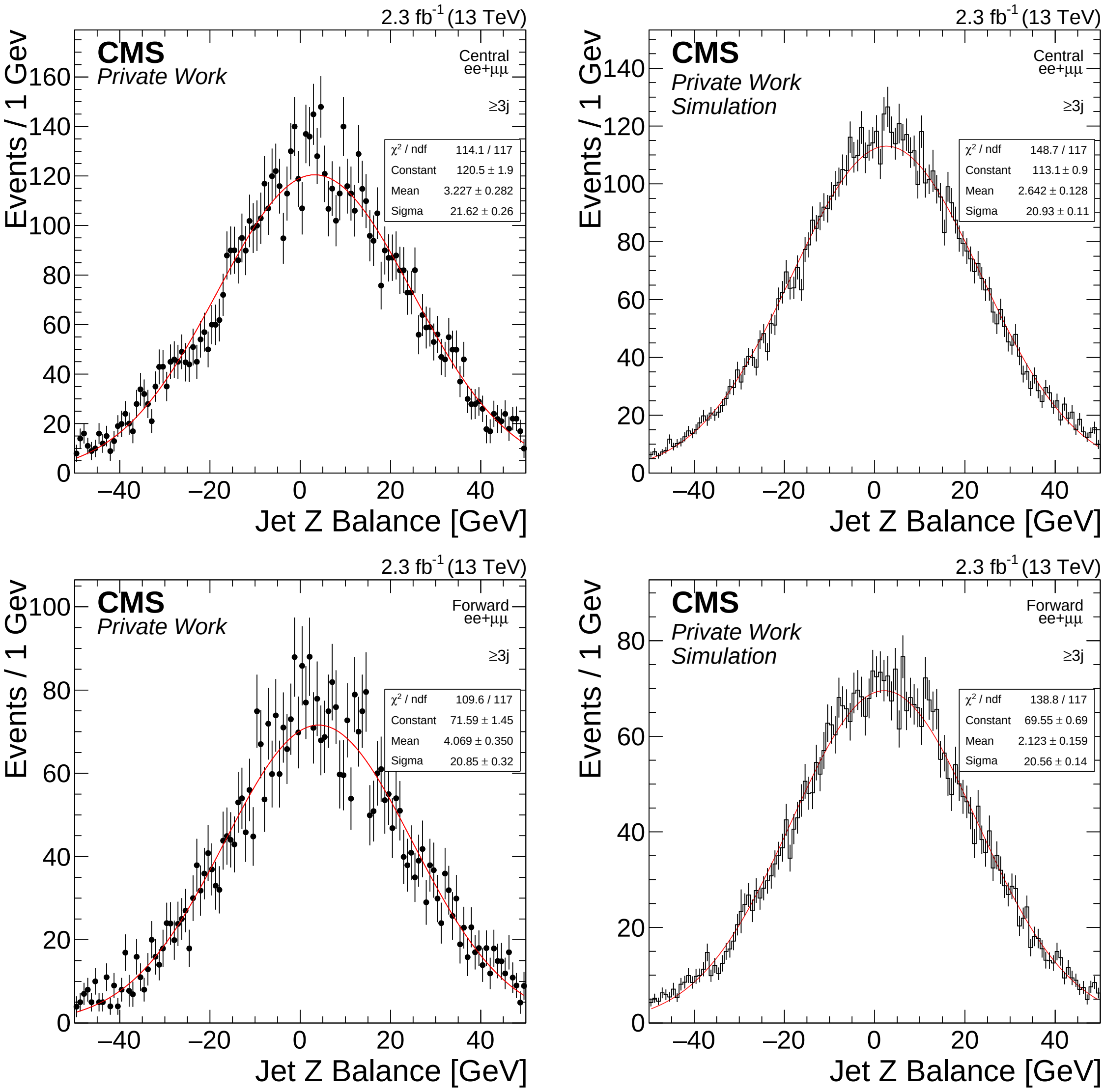

Figure 16: Gaussian fits to the JZB distributions in data (left) and simulation (right), considering the central (top) and forward (bottom) regions. Events with three or more jets are selected.

Propagation of JZB Corrections to E_T^{miss}

The JZB distribution, with JZB defined as in Eq. (6.20), is independent of the dilepton transverse momentum and pileup and is centered around zero. However, the corrections applied to JZB generate a mismatch between the E_T^{miss} spectra of JZB < 0 and JZB > 0. There is no mathematically motivated way of matching the E_T^{miss} spectra of JZB < 0 and JZB > 0 with JZB corrections applied, therefore an ansatz is used: The E_T^{miss} spectrum of JZB < 0 is corrected by "propagating" the JZB corrections in the following way:

$$E_T^{\text{miss}}(\text{JZB} < 0) \rightarrow E_T^{\text{miss}}(\text{JZB} < 0) - \alpha \cdot p_T^{\ell\ell} + \beta \cdot N_{\text{vertices}} + \mu \tag{6.21}$$

In this way, the relation $|\text{JZB}| < E_T^{\text{miss}}$ is restored. The effects of JZB corrections

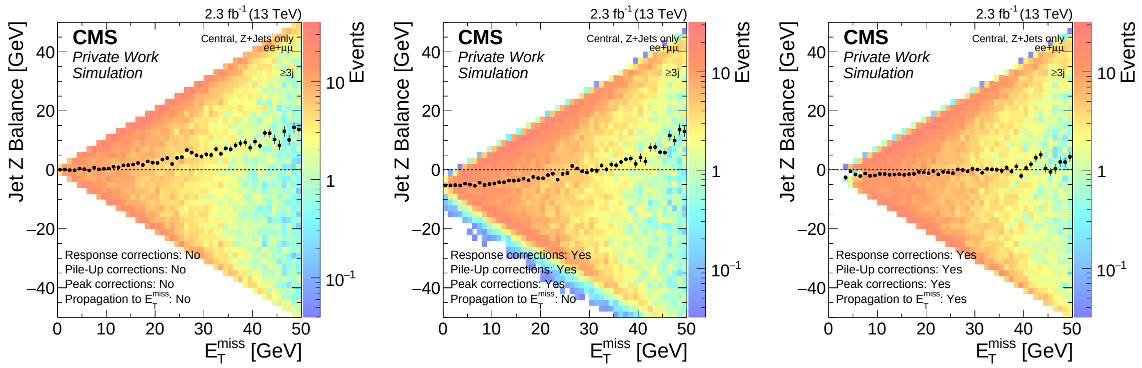

Figure 17: E_T^{miss}-JZB distributions with no corrections applied (left), corrections applied to JZB (middle) and JZB corrections "propagated" to E_T^{miss} for JZB $<$ 0. Simulated Z+jets events with three or more jets are selected.

and the "propagation" of the JZB corrections to the E_T^{miss} distribution of JZB < 0 are shown in Fig. 17. Through the JZB corrections, the number of events with JZB < 0 and JZB > 0 is equalized, but the JZB distribution is shifted with respect to the E_T^{miss} variable. By shifting the E_T^{miss} spectrum for JZB < 0 to higher values, it can be used for the estimation of the E_T^{miss} spectrum of JZB > 0.

Therefore, the prediction of Z+jets events is of the form

$$\begin{aligned} N_{SF}^{\text{Z+jets}}(\text{JZB} > 0, E_T^{\text{miss}} > X) = [&N_{SF}(\text{JZB} < 0, E_T^{\text{miss}} > X) \\ &-\text{R}_{\text{SF/OF}}{\cdot}N_{OF}(\text{JZB} < 0, E_T^{\text{miss}} > X)]_{\text{JZB corrected } E_T^{\text{miss}}} \end{aligned} \tag{6.22}$$

and thus

$$\begin{aligned} N_{SF}^{\text{Z+jets}}(E_T^{\text{miss}} > X) = [&N_{SF}(\text{JZB} < 0, E_T^{\text{miss}} > X) \\ &-\text{R}_{\text{SF/OF}}{\cdot}N_{OF}(\text{JZB} < 0, E_T^{\text{miss}} > X)]_{\text{JZB corrected } E_T^{\text{miss}}} \\ &+[N_{SF}(\text{JZB} < 0, E_T^{\text{miss}} > X) \\ &-\text{R}_{\text{SF/OF}}{\cdot}N_{OF}(\text{JZB} < 0, E_T^{\text{miss}} > X)]. \end{aligned} \tag{6.23}$$

The estimation in Eq. (6.23) is more complex than in Eq. (6.16) as it consists of two different parts. The first part is the prediction of the E_T^{miss} spectrum for JZB $>$ 0 through the spectrum of JZB $<$ 0 being matched to it, while the second part is the E_T^{miss} spectrum for JZB $<$ 0. For the second part, the JZB corrections are not propagated to E_T^{miss}. This is different from how the JZB method was employed in the past, where the part matched to the spectrum of JZB $>$ 0 was scaled by two. This change leads to smaller systematic uncertainties and better agreement between estimation and observation. When calculating statistical uncertainties, one has take into account that the two parts of the prediction have a large event overlap.

Closure tests on Z+jets Simulation for the E_T^{miss} spectrum prediction
To test the JZB method, closure tests on simulation are performed. In these closure tests, not the full estimation of Z+jets events, but the predictions as shown in Eq.(6.14) and Eq.(6.22) are tested. For the search in the dataset of 2015, this is performed with uncorrected and type-I corrected missing transverse energy. Only the Z+jets sample including DY $\rightarrow \tau\tau$ is used. For the search in the dataset of 2015, the closure test for the E_T^{miss} spectrum is shown, while the search in the dataset of 2016 is based on the JZB and thus does not need an estimation of the E_T^{miss} spectrum.

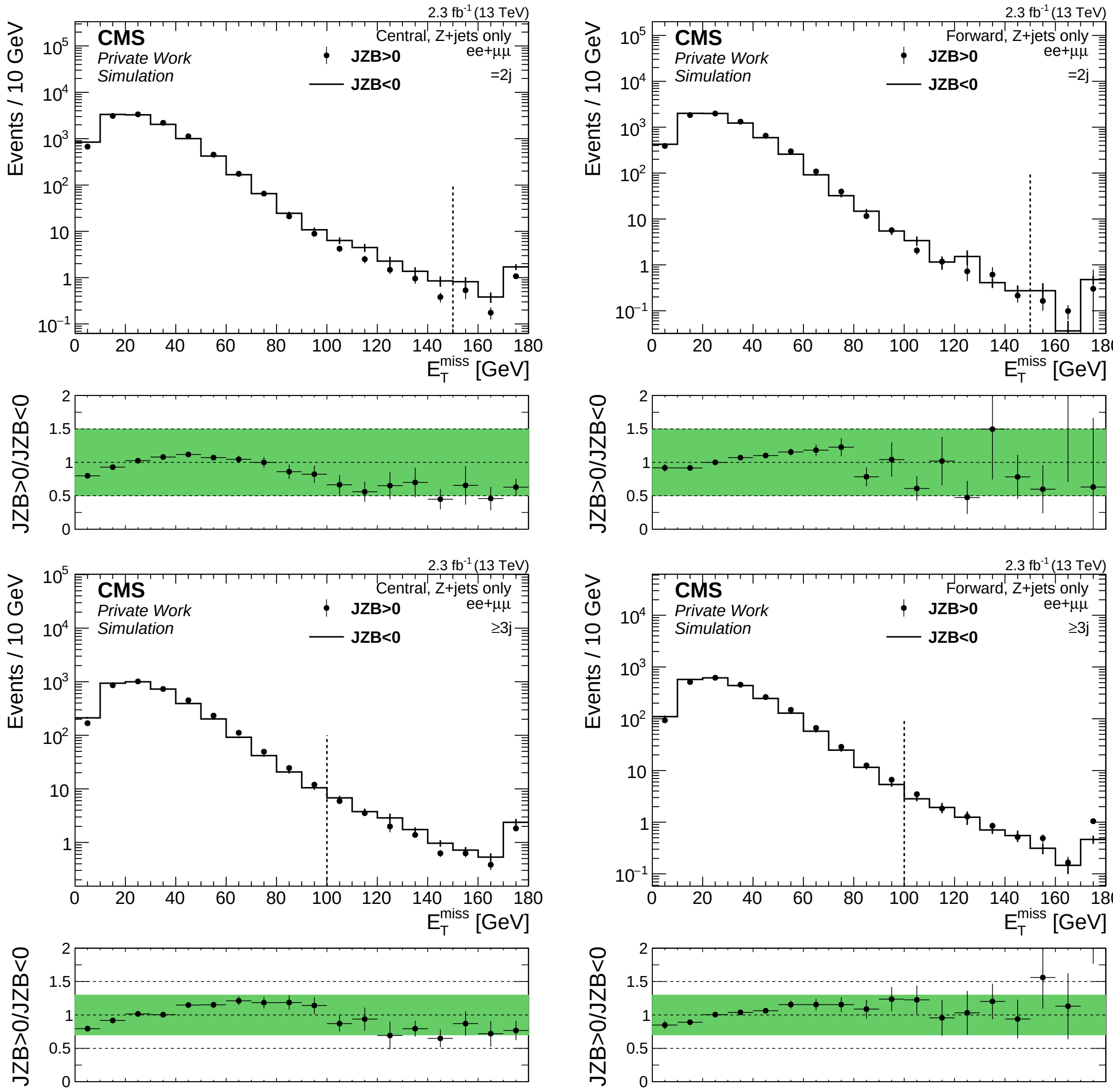

Figure 18: Closure tests of the E_T^{miss} spectra in the central (left) and forward (right) regions for two (top) and three or more (bottom) jets. $E_T^{\text{miss,type-I}}$ is used.

The closure tests for the search in the dataset of 2015 are shown in Fig. 18, using type-I corrected missing transverse energy. For high missing transverse energies, the JZB method performs better in events with three or more jets than in events with only two jets. This behavior is expected as the angular randomization of missing transverse energy with respect to the Z boson works better for higher jet multiplicities. The central and forward region show a different behavior for high missing transverse energies, as in the central region, the JZB method tends to do an overprediction of Z+jets events while there are tendencies to slight underpredictions in the forward region. The significantly worse closure in the case of two jets is less relevant as the E_T^{miss} requirement for events with two jets is more stringent than for events with three or more jets, resulting in a smaller contribution.

All closure tests show a curvature in the ratio plots for low missing transverse energies. This curvature is not expected and investigated by doing the closure tests with uncorrected missing transverse energy in Fig. 19.

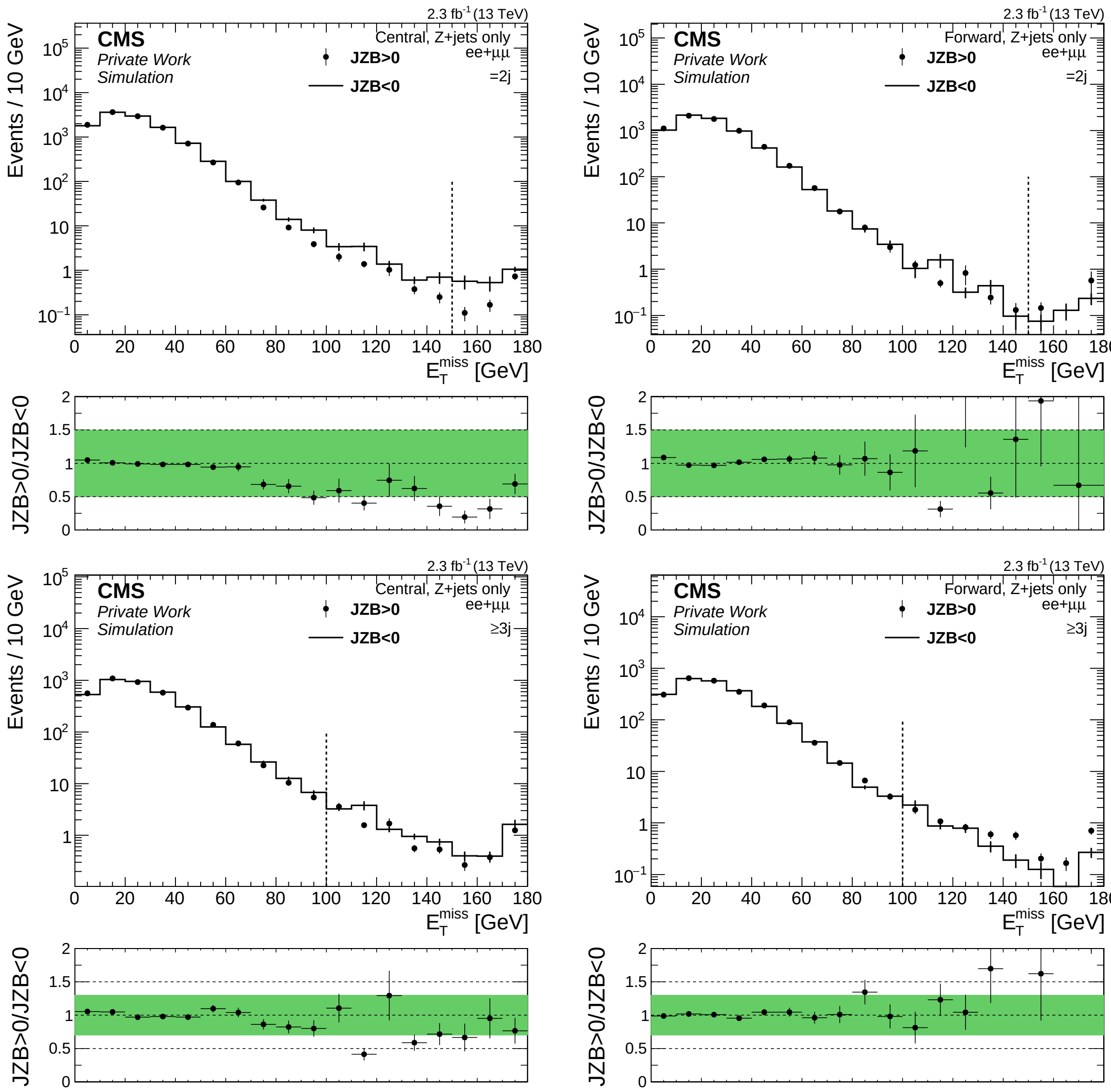

Figure 19: Closure tests of the E_T^{miss} spectra in the central (left) and forward (right) regions for two (top) and three or more (bottom) jets. $E_T^{\text{miss,uncorr}}$ is used.

Using uncorrected missing transverse energy, the agreement in the closure tests especially for low missing transverse energies is significantly better than when using type-I corrected missing transverse energy. This leads to the conclusion that type-I corrections introduce a bias into the prediction the E_T^{miss} spectrum when using the JZB method.

To confirm this, The difference between $E_T^{\text{miss,type-I}}$ and $E_T^{\text{miss,uncorr}}$ is plotted against the angle between $E_T^{\text{miss,uncorr}}$ and $p_T^{\ell\ell}$ in Fig. 20.

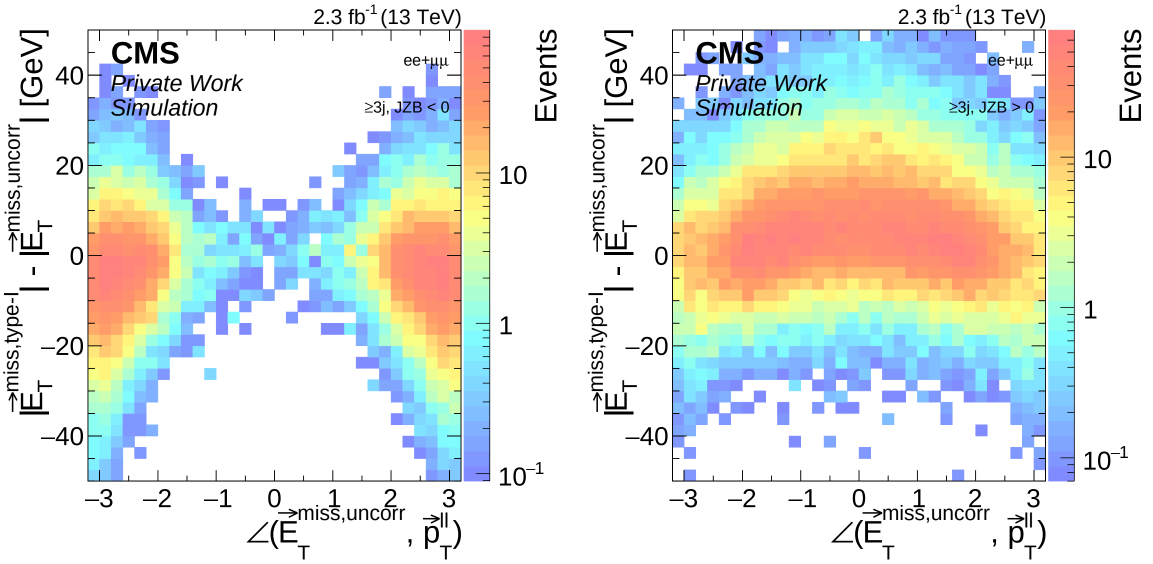

Figure 20: Two-dimensional distribution of the difference between $E_T^{\text{miss,type-I}}$ and $E_T^{\text{miss,uncorr}}$ and the angle between $E_T^{\text{miss,uncorr}}$ and $p_T^{\ell\ell}$ for JZB < 0 (left) and JZB > 0 (right).

For events with JZB < 0, the type-I corrections tend to reduce the missing transverse energy while the opposite is the case for JZB > 0. This explains the curvature seen for low missing transverse energies in the E_T^{miss} closure tests. As type-I corrections correct for the detector response, they tend to correct jet energies to higher energies. Negative values of JZB occur if $\vec{E}_T^{\text{miss}}$ and $p_T^{\ell\ell}$ are antiparallel, which usually occurs if the mismeasured jet is parallel to $p_T^{\ell\ell}$. In this case, type-I corrections reduce the missing transverse energy by increasing the jet energy. The opposite scenario is the case for positive values of JZB. This way, type-I corrections introduce a bias in the prediction of the E_T^{miss} spectrum.

The introduced bias is most relevant for low values of E_T^{miss} and the closure for high values of E_T^{miss} is similar in $E_T^{\text{miss,type-I}}$ and $E_T^{\text{miss,uncorr}}$. As other systematic effects like the tendency for overpredictions are larger, this effect is not dealt with. To cover the differences in closure, a systematic uncertainty of 30 % (50 %) is applied to the prediction in events with three or more (exactly two) jets. This uncertainty is only applied to the part of the estimation that is used to predict the E_T^{miss} spectrum of events with JZB > 0 as the other part of the estimation is by definition exact. An additional, mostly negligible, systematic uncertainty emerges from the OF subtraction using $R_{\text{SF/OF}}$. It is applied to the total prediction through error propagation.

The complete closure test in the signal regions is given in Table 13.

Good agreement within the uncertainties is observed in most regions. The most relevant region "on Z" shows the expected tendencies of over- and underprediction,

Table 13: Estimated and Observed event yields in the signal regions in simulation.

	Low Mass		Below Z		On Z		Above Z		High Mass	
	Predicted	Obs.	Predicted	Obs.	Predicted	Obs.	Predicted	Obs.	Predicted	Obs.
Central	3.2 ± 1.0	3.8 ± 0.5	1.5 ± 0.5	2.4 ± 0.5	45.3 ± 8.3	40.2 ± 1.5	1.9 ± 0.6	1.2 ± 0.2	0.9 ± 0.3	1.7 ± 0.2
Forward	0.9 ± 0.3	2.8 ± 0.7	0.6 ± 0.2	1.1 ± 0.2	15.3 ± 3.6	19.1 ± 1.0	0.7 ± 0.2	1.1 ± 0.2	0.4 ± 0.1	0.8 ± 0.1

but estimation and observation are compatible. For data, significantly higher statistical uncertainties are to be expected, covering the differences seen in simulation.

Closure tests on Z+jets Simulation for the JZB spectrum prediction

For the prediction of the JZB spectrum, the previously mentioned bias from type-I corrections is not relevant. The shown closure test is performed in the signal region of the search in the dataset of 2016 with all requirements but the JZB $> 225\,\text{GeV}$ requirement applied. Again, only simulated Z+jets events are used. To compare the negative and positive JZB spectra, the negative JZB spectrum is multiplied by -1. The closure test is shown in Fig. 21.

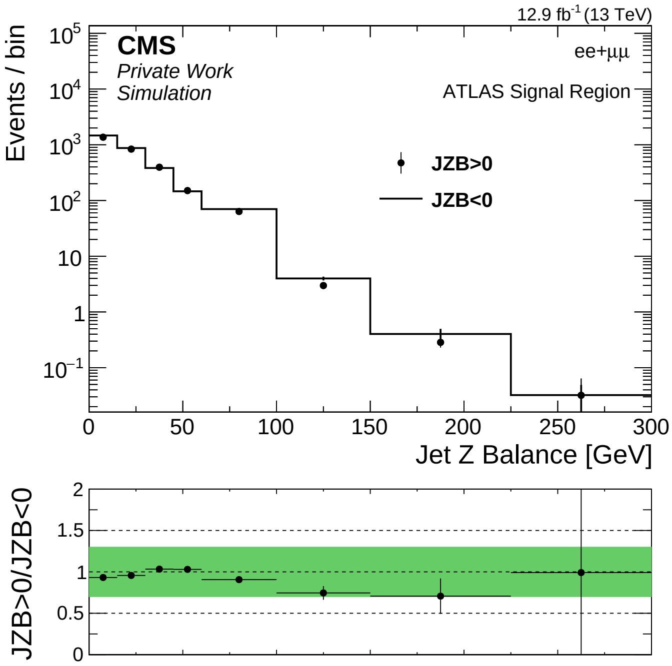

Figure 21: Closure test of the Z+jets prediction in simulation.

For high values of |JZB|, the statistical significance of the simulated samples is low. Over the entire spectrum, an agreement within 30 % is observed. Therefore, a systematic uncertainty of 30 % is applied to the prediction.

Signal Contamination Studies for the search in the dataset of 2015

Depending on the masses of $\tilde{b}$ and $\tilde{\chi}_2^0$, a certain fraction of signal events is expected to have negative values of JZB. If that fraction becomes 50 % or higher, the JZB method loses any sensitivity to the SUSY signal as it includes these events in the background prediction. Depending on the mass difference between the SUSY particles, the JZB distribution and the dileptonic mass distribution of the signal model are expected to change. In Fig. 22 the ratio of signal events with negative values of JZB in the inclusive "on Z" signal region is depicted for all simulated masses of $\tilde{b}$ and $\tilde{\chi}_2^0$.

For low $\tilde{\chi}_2^0$ masses, the fraction of events with negative values of JZB is about 20 % and increases to up to 60 % for high $\tilde{\chi}_2^0$ masses close to the diagonal. To estimate the impact of this, the fraction of signal events misidentified as Z+jets background and the total number of signal events in the signal region is shown in Fig. 23. For $\tilde{\chi}_2^0$ masses below 200 GeV, no signal events in the "on Z" region are expected.

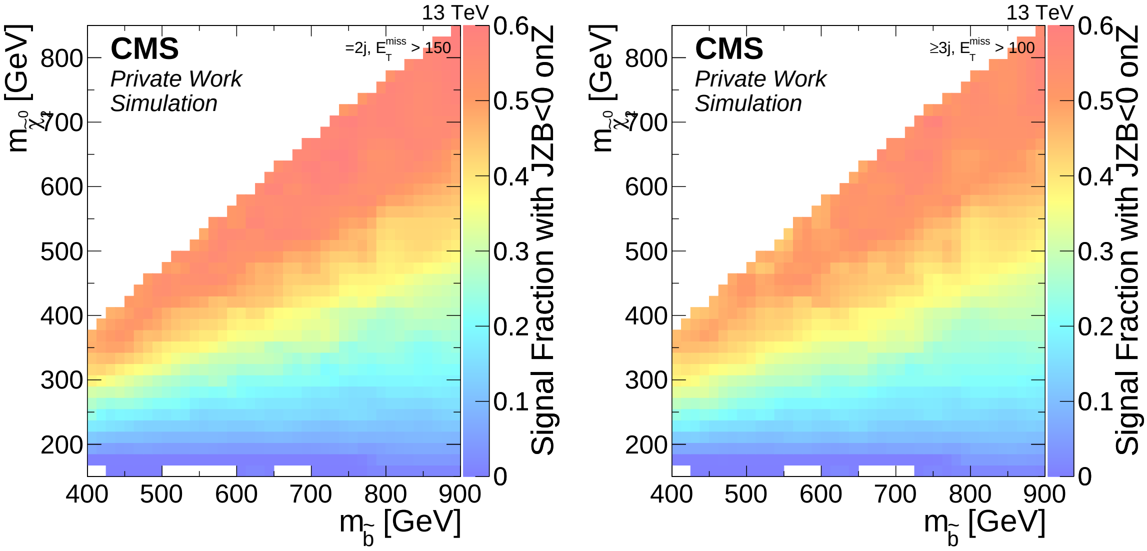

Figure 22: Fractions of signal events on Z with JZB <0 for events with two (left) and three or more (right) jets.

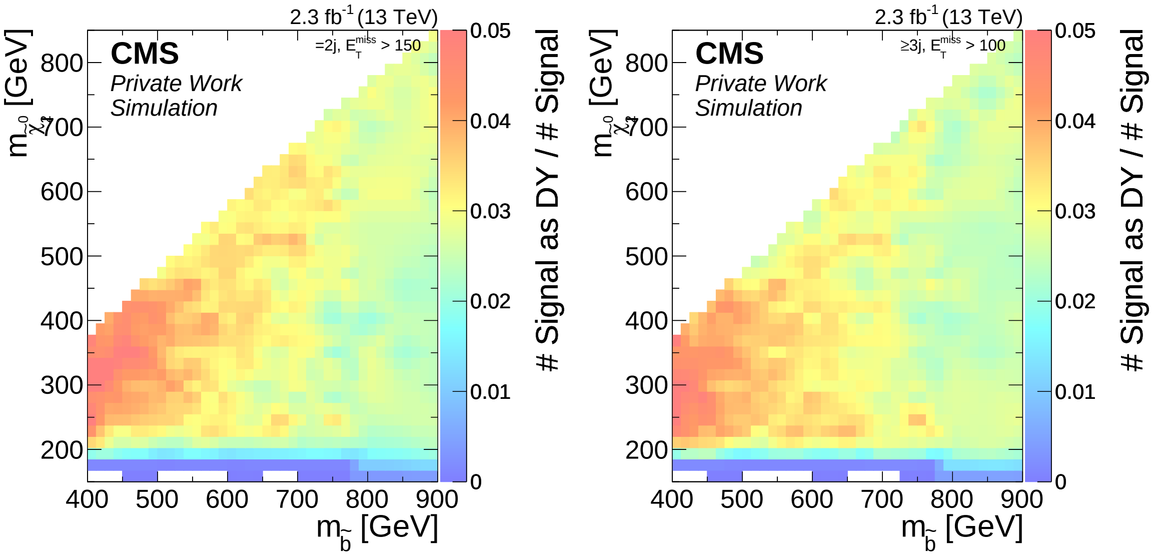

Figure 23: Ratio of signal events misidentified as Z+jets events and total number of signal events in the signal region for events with two (left) and three or more (right) jets.

The fraction of signal events misidentified as Z+jets background is negligible for most signal samples, only reaching 5 % for low $\tilde{b}$ masses. Therefore, signal contamination has a small effect on the JZB method for the T6bbllslepton model as signal events do not populate the Z peak for most sparticle masses.

6.2.2 E_T^{miss}-Template Method

The E_T^{miss}-template method is a data-driven method of estimating the E_T^{miss} spectrum of the Z+jets background. It was used and combined with the JZB method in the search for SUSY performed on the dataset of 2012 [5] and is the only Z+jets background estimation method used in the published search with data taken in 2015 [6]. This method is not applied in this thesis, but its results are compared to those of the JZB method. Therefore, a basic description of the method is given.

The E_T^{miss}-template method uses the similarity between γ+jets and Z+jets events to estimate the E_T^{miss} spectrum produced in Z+jets events. In Z+jets events, the missing transverse energy is generated by the mismeasurement of jet energies, while the Z boson (more precisely, its decay products) is well measured. A similar event structure exists in γ+jets events, where the well-measured photon recoils against jets. The idea of the E_T^{miss} templates method is to extract the E_T^{miss} spectrum generated in Z+jets events from γ+jets events.

Therefore, a control data sample taken with various photon triggers requiring photon transverse momenta thresholds between 22 and 165 GeV is used for this estimation method. Basic photon selection requirements are applied. As there are kinematical differences between the γ+jets and Z+jets process, the p_T of the photon is reweighted to match that of the Z boson ($p_T^{\ell\ell}$). The resulting E_T^{miss} spectrum is then normalized in a Drell-Yan enriched region ($E_T^{\text{miss}} < 50\,\text{GeV}$) to match the number of dileptonic events in this region.

Systematic uncertainties of this methods arise from closure tests performed on simulated samples, the normalization done in the Drell-Yan enriched region, and the photon selection criteria. Typical systematic uncertainties in the signal region used for the 2015 search are between 10 and 30 %.

6.3 Other Backgrounds

Certain SM processes are not covered by the previous background estimation methods. These backgrounds are only relevant for the dedicated search performed in the data taken in 2016. Using simulated samples of various SM processes, it is found that the decay WZ $\rightarrow 3\ell 1\nu$ makes a significant contribution to the signal region and cannot be estimated by the other background prediction methods. Therefore, the contribution is estimated using a simulated sample. The simulated sample is validated in a three-lepton control region. The third lepton is required to have $p_T > 10\,\text{GeV}$ and needs to pass loose isolation requirements. Additionally, a E_T^{miss} threshold of 60 GeV and a veto on b-tagged jets with $p_T > 25\,\text{GeV}$ are applied. This validation is done for another search [52] and not specifically for this thesis. It is shown in Fig. 24.

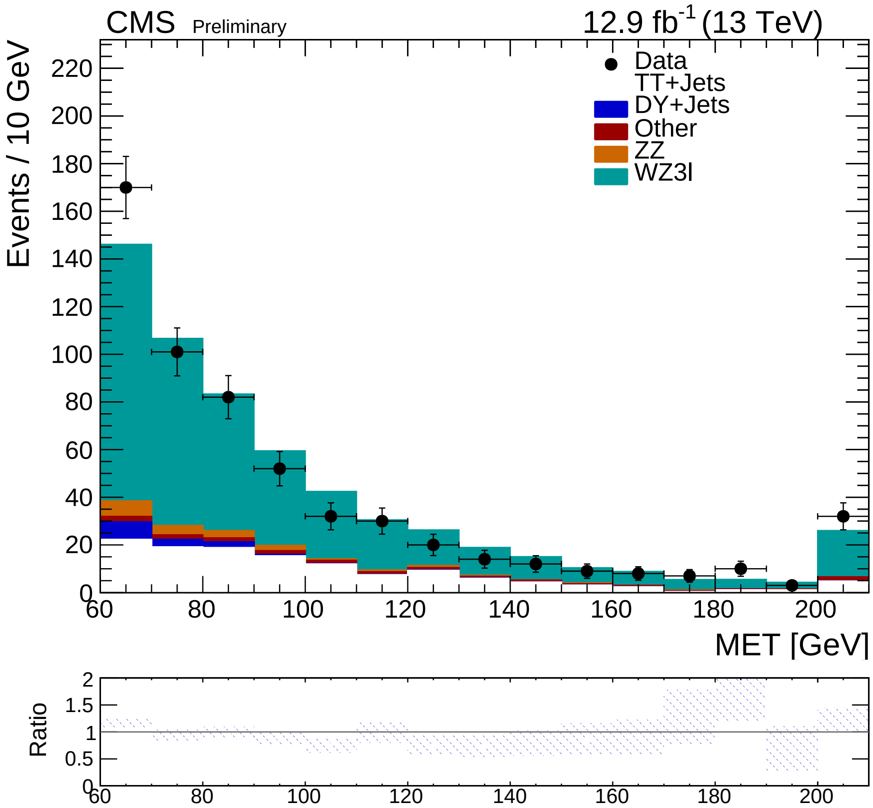

Figure 24: Validation of the simulated WZ $\rightarrow 3\ell 1\nu$ sample in a control region [52].

The agreement between data and simulation is sufficient. To account for possible differences in the signal region, a conservative uncertainty of 50 % is applied to the prediction.

7 Results

With the JZB method established and the estimation of other SM backgrounds covered, the estimations can be compared to the selected events in data.

7.1 Estimation of Z+jets events in signal region for the 2015 search

The estimation of Z+jets events in the signal region is performed using Eq. (6.23). It is compared to the published results that were obtained using the E_T^{miss}-template method. The results are only compared in the dilepton mass region "on Z" ($81 < m_{\ell\ell} < 101\,\text{GeV}$) as both methods use the $R_{\text{out/in}}$ method for extrapolation to other mass regions. The Z+jets background estimations using the JZB method and the E_T^{miss}-template method [6] are shown in Table 14.

Table 14: Comparison of the Z+jets estimation for both methods.

Region	E_T^{miss}-template method	JZB method
Central	62 ± 8	64 ± 21
Forward	24 ± 3	21 ± 10

The results show good agreement, with a slightly higher estimation in the central region and a slightly lower estimation in the forward region. This behavior was also seen in the closure tests on simulation. The uncertainties obtained using the JZB methods are significantly larger as the JZB method effectively scales the number of events with JZB < 0 by about 2. Therefore, the statistical uncertainties for the results using the JZB method are of the order $2 \cdot \sqrt{N}$. For larger integrated luminosities and higher numbers of Z+jets events in the signal region, the statistical uncertainties become less relevant and the systematic uncertainties, which are expected to be of a similar order as those using E_T^{miss} templates, are dominant. Systematic and statistical uncertainties are of the same order at integrated luminosities of more than $7\,\text{fb}^{-1}$ (in the central region, assuming a 15 % systematic uncertainty on the total prediction). At about $20\,\text{fb}^{-1}$, the statistical uncertainties are expected to be around 5 % (in the central region), resulting in a total uncertainty dominated by the systematic uncertainty.

The resulting total background estimation for the signal region of the 2015 search is shown in Fig. 25.

The shape of the Z+jets estimation in these figures is extracted from the dilepton mass distribution of events in the Drell-Yan enriched region, scaling it so the number of events in the on Z region matches the estimation made with the JZB method. This is an implicit application of the $R_{\text{out/in}}$ scale factor to the off Z regions, thus a 25 % systematic uncertainty is applied in those regions. The agreement of estimation and observed data is good on the Z peak. The slight excess of events at low masses in the

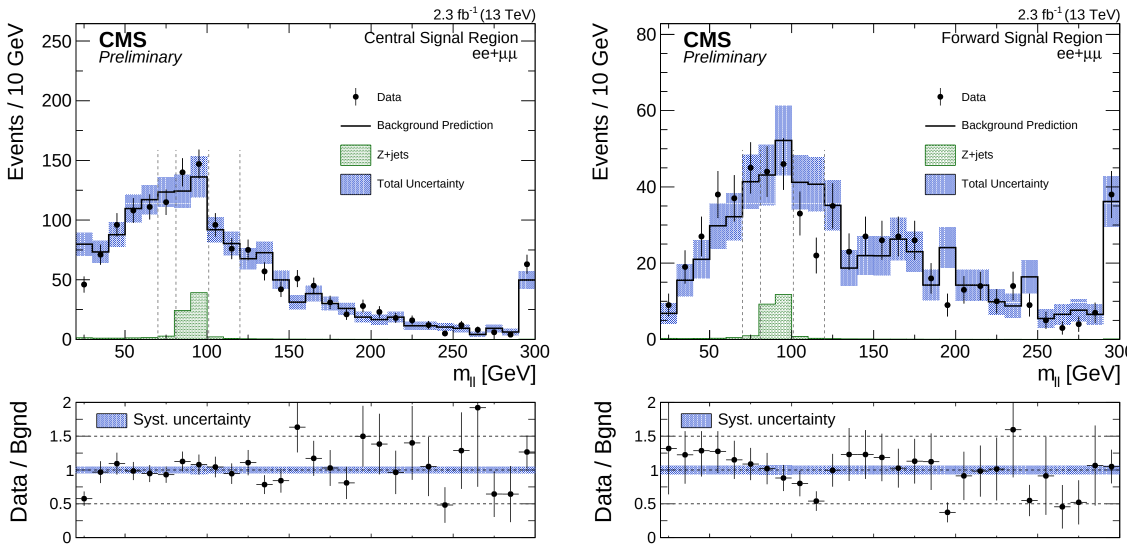

Figure 25: Background estimation in the central (left) and forward (right) signal regions. Only the contributions by flavor-symmetric and Z+jets backgrounds are accounted for.

forward region was observed in the published results as well and is insignificant due to the low number of events.

In summary, the JZB method is suitable to be used for the estimation of the Z+jets background. Using a larger dataset, the JZB method can yield uncertainties of a similar size as the E_T^{miss}-template method. On the relatively small set of data taken in 2015, it can be considered a statistically independent cross-check to the published results, which it confirms.

7.2 Background estimation in the signal region for the 2016 search

The background estimation for the search for SUSY in data taken in 2016 includes the estimation of all SM backgrounds. While the Z+jets background is estimated using the JZB method, FS backgrounds are estimated with the $\text{R}_{\text{SF/OF}}$ method and other processes are estimated by simulation, thus the estimation is of the form

$$N_{SF}(\text{JZB} > X) = N_{SF}(\text{JZB} < -X) - \text{R}_{\text{SF/OF}} \cdot N_{OF}(\text{JZB} < -X) + \text{R}_{\text{SF/OF}} \cdot N_{OF}(\text{JZB} > X) + N_{\text{other}}^{\text{Simulation}}. \tag{7.1}$$

The results are shown in Table 15.

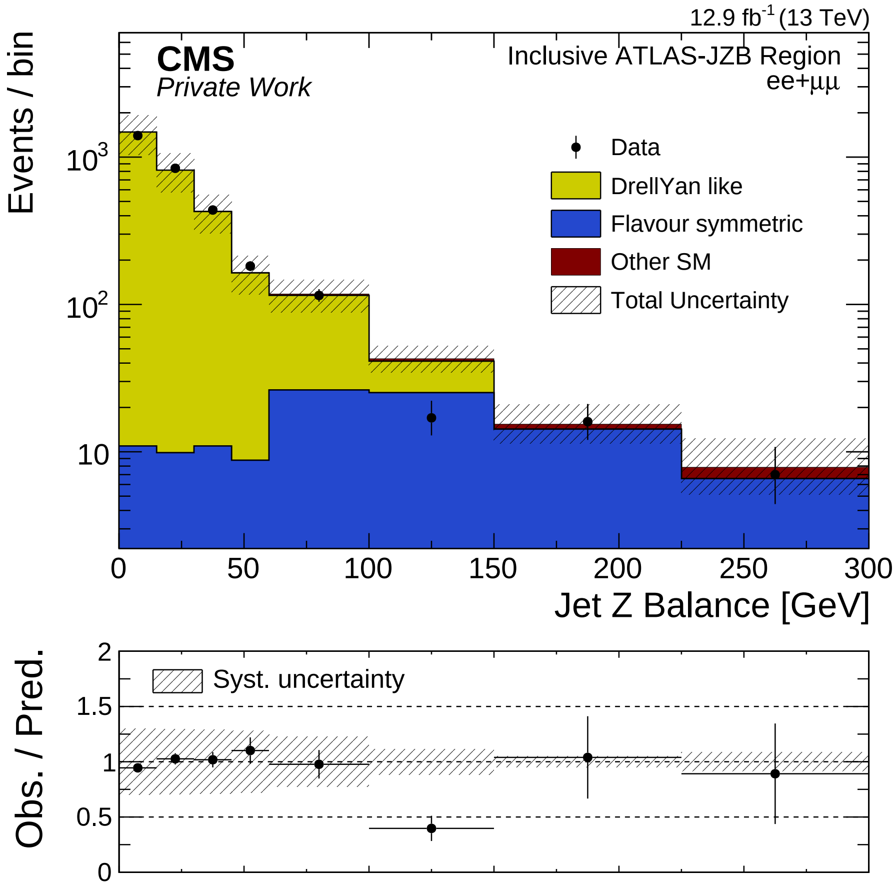

Figure 26: Comparison of observed and predicted data. The last bin is the signal region bin.

Table 15: Observed and expected numbers of events in the signal region used in 2016

FS Background	$6.5^{+3.9}_{-2.6}$
Z+Jets	$0.0^{+1.8}_{-0}$
Other SM	$1.2^{+0.6}_{-0.6}$
Total Background	$7.7^{+4.3}_{-2.7}$
Observed	7

Figure 26 shows an overall good agreement of the observed and estimated events. Though a slight overprediction of events in the signal region is seen, the estimation of backgrounds is compatible with the observed events within the uncertainties. No Z+jets events are predicted in the signal region, therefore a Poisson interval is given for the upper limit on the number of Z+jets events. Because of the expected shape of the JZB distribution of Z+jets events, this upper limit is probably overestimated. Using information about the JZB distribution, it might be possible to estimate a more realistic upper limit on the number of Z+jets events.

Due to different frameworks being used, the shown event yields are different from the published results [52] by 1-2 events in both estimation and observation. However, in neither of the analyses a significant excess was found, thus the differences are not problematic.

In summary, the excess found by ATLAS in a similar signal region cannot be confirmed by this search as good agreement between observation and prediction is observed. In a similar search using the E_T^{miss}-template method [6, 52], no excess over the SM expectations was found, either.

8 Summary and Outlook

In this thesis, the JZB method was introduced and applied for the estimation of Z+jets backgrounds. This was motivated by establishing a statistically independent alternative to the E_T^{miss}-template method. As the JZB distribution is symmetric around zero for Z+jets events but prefers positive values for processes with genuine missing transverse energy, the number of Z+jets background events can be estimated from the number of events with negative values of JZB. As the JZB method was found to obtain reliable results, a search was performed to examine a signal region in which the ATLAS collaboration had previously found an excess over SM expectations in two independent data sets. No significant excess over the SM expectations was found in the signal region using the JZB method on data taken in 2016. In September 2016, the ATLAS collaboration published results on data taken in 2016 and reported that no new excess in the signal region was observed [60]. Thus, it can be assumed that the previously reported excesses are statistical fluctuations.

The JZB method is found to obtain large statistical uncertainties when used for the estimation of the E_T^{miss} spectrum of Z+jets events, therefore it is more suitable to be used in a dedicated search with a signal region defined by a JZB threshold. Doing this also gives the advantage of not having systematic effects from type-I E_T^{miss} corrections introducing a bias into the estimation. For signal regions with zero estimated Z+jets events, the JZB methods in its current state provides large uncertainties. To improve the JZB method, the estimation of upper limits on the estimation in such regions needs to be optimized.

Whether it is reasonable to permanently use the JZB method to be combined with the E_T^{miss}-template method is not clear. Despite a large amount of data being collected in 2016, the number of Z+jets events expected in the signal regions does not increase as much due to higher requirements on the missing transverse energy in the signal region definition (now $E_T^{\text{miss}} > 150\,\text{GeV}$) [52] in comparison to the published analysis on the dataset of 2015. Therefore, further studies have to be made to see if one can obtain results with similar uncertainties when using the JZB method as when using the E_T^{miss}-template method.

The JZB method provides an independent estimation of the Z+jets background contribution. The signal contamination considering the "T6bbllslepton" scenario is not problematic. With a large enough dataset, the statistical uncertainties become small enough for the JZB method to be competitive with the E_T^{miss}-template method.

A List of used Datasets

The datasets taken in 2015 are composed of runs with numbers between 246908 and 260627. The runs used are listed in the json file Cert_246908-260627_13TeV_PromptReco_Collisions15_25ns_JSON_v2.txt. The used datasets are listed in Table A.1.

Table A.1: Used datasets for data taken in 2015

Dataset
/DoubleEG/Run2015B-PromptReco-v1/MINIAOD
/DoubleEG/Run2015C-PromptReco-v1/MINIAOD
/DoubleEG/Run2015D-PromptReco-v3/MINIAOD
/DoubleMuon/Run2015B-PromptReco-v1/MINIAOD
/DoubleMuon/Run2015C-PromptReco-v1/MINIAOD
/DoubleMuon/Run2015D-PromptReco-v3/MINIAOD
/MuonEG/Run2015B-PromptReco-v1/MINIAOD
/MuonEG/Run2015C-PromptReco-v1/MINIAOD
/MuonEG/Run2015D-PromptReco-v3/MINIAOD

The json file used for the dataset of 2016 is Cert_271036-279588_13TeV_PromptReco_Collisions16_JSON_NoL1T.txt. The used datasets are listed in Table A.2.

Table A.2: Used datasets for data taken in 2016

Dataset
/DoubleEG/Run2016B-PromptReco-v2/MINIAOD
/DoubleEG/Run2016C-PromptReco-v2/MINIAOD
/DoubleEG/Run2016D-PromptReco-v2/MINIAOD
/DoubleMuon/Run2016B-PromptReco-v2/MINIAOD
/DoubleMuon/Run2016C-PromptReco-v2/MINIAOD
/DoubleMuon/Run2016D-PromptReco-v2/MINIAOD
/MuonEG/Run2016B-PromptReco-v2/MINIAOD
/MuonEG/Run2016C-PromptReco-v2/MINIAOD
/MuonEG/Run2016D-PromptReco-v2/MINIAOD

The triggers used for the datasets of 2015 and 2016 are listed in Table A.3 and Table A.4. The trigger paths signify that the used triggers are high level trigger and give information about the requirements set by the trigger. For example, Mu17 indicates that the trigger requires a muon to have $p_T > 17\,\mathrm{GeV}$ in order for it to pass the trigger requirements. Other requirements on isolation and the impact parameter are also included in certain trigger paths.

Table A.3: Used triggers for the dataset of 2015

Trigger Path
HLT_Mu17_TrkIsoVVL_Mu8_TrkIsoVVL_DZ_v*
HLT_Mu17_TrkIsoVVL_TkMu8_TrkIsoVVL_DZ_v*
HLT_Ele17_Ele12_CaloIdL_TrackIdL_IsoVL_DZ_v*
HLT_Mu8_TrkIsoVVL_Ele17_CaloIdL_TrackIdL_IsoVL_v*
HLT_Mu17_TrkIsoVVL_Ele12_CaloIdL_TrackIdL_IsoVL_v*
HLT_Mu27_TkMu8_v*
HLT_Mu30_Ele30_CaloIdL_GsfTrkIdVL_v*
HLT_DoubleEle33_CaloIdL_GsfTrkIdVL_v*
Baseline triggers for trigger efficiency measurements
HLT_PFHT200_v*
HLT_PFHT250_v*
HLT_PFHT300_v*
HLT_PFHT350_v*
HLT_PFHT400_v*
HLT_PFHT475_v*
HLT_PFHT600_v*
HLT_PFHT650_v*
HLT_PFHT800_v*
HLT_PFHT900_v*
HLT_Photon22_R9Id90_HE10_IsoM_v*
HLT_Photon30_R9Id90_HE10_IsoM_v*
HLT_Photon36_R9Id90_HE10_IsoM_v*
HLT_Photon50_R9Id90_HE10_IsoM_v*
HLT_Photon75_R9Id90_HE10_IsoM_v*
HLT_Photon90_R9Id90_HE10_IsoM_v*
HLT_Photon120_R9Id90_HE10_IsoM_v*
HLT_Photon165_R9Id90_HE10_IsoM_v*

Table A.4: Used triggers for the dataset of 2016

Trigger Path
HLT_Mu17_TrkIsoVVL_Mu8_TrkIsoVVL_v*
HLT_Mu17_TrkIsoVVL_TkMu8_TrkIsoVVL_v*
HLT_Ele17_Ele12_CaloIdL_TrackIdL_IsoVL_DZ_v*
HLT_Ele23_Ele12_CaloIdL_TrackIdL_IsoVL_DZ_v*
HLT_Mu8_TrkIsoVVL_Ele17_CaloIdL_TrackIdL_IsoVL_v*
HLT_Mu8_TrkIsoVVL_Ele23_CaloIdL_TrackIdL_IsoVL_v*
HLT_Mu17_TrkIsoVVL_Ele12_CaloIdL_TrackIdL_IsoVL_v*
HLT_Mu23_TrkIsoVVL_Ele12_CaloIdL_TrackIdL_IsoVL_v*
HLT_Mu27_TkMu8_v*
HLT_Mu30_TkMu11_v*
HLT_Mu30_Ele30_CaloIdL_GsfTrkIdVL_v*
HLT_DoubleEle33_CaloIdL_GsfTrkIdVL_v*
Baseline triggers for trigger efficiency measurements
HLT_PFHT125_v*
HLT_PFHT200_v*
HLT_PFHT250_v*
HLT_PFHT300_v*
HLT_PFHT350_v*
HLT_PFHT400_v*
HLT_PFHT475_v*
HLT_PFHT600_v*
HLT_PFHT650_v*
HLT_PFHT800_v*
HLT_PFHT900_v*

B Simulated Datasets

The used simulated datasets are listed in Table B.1 and Table B.2. Samples that were used to estimate the relevant SM backgrounds but were not used in the analysis are left out. As the Drell-Yan samples binned in hadronic activity do not include samples with $H_T < 100\,\text{GeV}$, inclusive samples were used for this hadronic activity range, applying an upper treshold on the generated hadronic activity. In events with two jets, this sample only has a small effect, in events with three or more jets, there is no visible contribution by the inclusive sample. Because of the requirements on hadronic activity in the signal region used for the dataset of 2016, there is no contribution by the inclusive sample even in events with two jets.

The SUSY signal samples include different $\tilde{\text{b}}$ masses which lead to different cross sections. Their cross sections at 13 TeV are listed in Table B.3.

Table B.1: Used simulated datasets for data taken in 2015

Dataset path	σ [pb]
$\text{t}\bar{\text{t}}$ datasets	
/TTTo2L2Nu_13TeV-powheg/RunIISpring15MiniAODv2-74X_mcRun2_asymptotic_v2-v1/MINIAODSIM [61]	87.31
Drell-Yan datasets	
/DYJetsToLL_M-50_TuneCUETP8M1_13TeV-madgraphMLM-pythia8/RunIISpring15MiniAODv2-74X_mcRun2_asymptotic_v2-v1/MINIAODSIM	6025.2
/DYJetsToLL_M-5to50_TuneCUETP8M1_13TeV-madgraphMLM-pythia8/RunIISpring15MiniAODv2-74X_mcRun2_asymptotic_v2-v1/MINIAODSIM	18610
/DYJetsToLL_M-50_HT-100to200_TuneCUETP8M1_13TeV-madgraphMLM-pythia8/RunIISpring15MiniAODv2-74X_mcRun2_asymptotic_v2-v1/MINIAODSIM	147.4
/DYJetsToLL_M-50_HT-200to400_TuneCUETP8M1_13TeV-madgraphMLM-pythia8/RunIISpring15MiniAODv2-74X_mcRun2_asymptotic_v2-v1/MINIAODSIM	40.99
/DYJetsToLL_M-50_HT-400to600_TuneCUETP8M1_13TeV-madgraphMLM-pythia8/RunIISpring15MiniAODv2-74X_mcRun2_asymptotic_v2-v2/MINIAODSIM	5.678
/DYJetsToLL_M-50_HT-600toInf_TuneCUETP8M1_13TeV-madgraphMLM-pythia8/RunIISpring15MiniAODv2-74X_mcRun2_asymptotic_v2-v1/MINIAODSIM	2.198
/DYJetsToLL_M-5to50_HT-100to200_TuneCUETP8M1_13TeV-madgraphMLM-pythia8/RunIISpring15MiniAODv2-74X_mcRun2_asymptotic_v2-v1/MINIAODSIM	224.2
/DYJetsToLL_M-5to50_HT-200to400_TuneCUETP8M1_13TeV-madgraphMLM-pythia8/RunIISpring15MiniAODv2-74X_mcRun2_asymptotic_v2-v1/MINIAODSIM	37.2
/DYJetsToLL_M-5to50_HT-400to600_TuneCUETP8M1_13TeV-madgraphMLM-pythia8/RunIISpring15MiniAODv2-74X_mcRun2_asymptotic_v2-v1/MINIAODSIM	3.581
/DYJetsToLL_M-5to50_HT-600toInf_TuneCUETP8M1_13TeV-madgraphMLM-pythia8/RunIISpring15MiniAODv2-74X_mcRun2_asymptotic_v2-v1/MINIAODSIM	1.124
T6bbllslepton datasets	
/SMS-T6bbllslepton_mSbottom-400To575_mLSP-150To550_TuneCUETP8M1_13TeV-madgraphMLM-pythia8/RunIISpring15MiniAODv2-FastAsympt25ns_74X_mcRun2_asymptotic_v2-v1/MINIAODSIM	varying
/SMS-T6bbllslepton_mSbottom-600To775_mLSP-150To725_TuneCUETP8M1_13TeV-madgraphMLM-pythia8/RunIISpring15MiniAODv2-FastAsympt25ns_74X_mcRun2_asymptotic_v2-v1/MINIAODSIM	varying
/SMS-T6bbllslepton_mSbottom-800To950_mLSP-150To900_TuneCUETP8M1_13TeV-madgraphMLM-pythia8/RunIISpring15MiniAODv2-FastAsympt25ns_74X_mcRun2_asymptotic_v2-v1/MINIAODSIM	varying

Table B.2: Used simulated datasets for data taken in 2016

Dataset path	σ [pb]
$t\bar{t}$ datasets	
/TTTo2L2Nu_13TeV-powheg/RunIISpring16MiniAODv2-PUSpring16_80X_mcRun2_asymptotic_2016_miniAODv2_v0_ext1-v1/MINIAODSIM [61]	87.31
Drell-Yan datasets	
/DYJetsToLL_M-50_TuneCUETP8M1_13TeV-madgraphMLM-pythia8/RunIISpring16MiniAODv2-PUSpring16_80X_mcRun2_asymptotic_2016_miniAODv2_v0_ext1-v1/MINIAODSIM	6025.2
/DYJetsToLL_M-50_HT-100to200_TuneCUETP8M1_13TeV-madgraphMLM-pythia8/RunIISpring16MiniAODv2-PUSpring16_80X_mcRun2_asymptotic_2016_miniAODv2_v0_ext1-v1/MINIAODSIM	139.4
/DYJetsToLL_M-50_HT-200to400_TuneCUETP8M1_13TeV-madgraphMLM-pythia8/RunIISpring16MiniAODv2-PUSpring16_80X_mcRun2_asymptotic_2016_miniAODv2_v0_ext1-v1/MINIAODSIM	42.75
/DYJetsToLL_M-50_HT-400to600_TuneCUETP8M1_13TeV-madgraphMLM-pythia8/RunIISpring16MiniAODv2-PUSpring16_80X_mcRun2_asymptotic_2016_miniAODv2_v0_ext1-v1/MINIAODSIM	5.497
/DYJetsToLL_M-50_HT-600toInf_TuneCUETP8M1_13TeV-madgraphMLM-pythia8/RunIISpring16MiniAODv2-PUSpring16_80X_mcRun2_asymptotic_2016_miniAODv2_v0_ext1-v1/MINIAODSIM	2.21
/DYJetsToLL_M-5to50_HT-100to200_TuneCUETP8M1_13TeV-madgraphMLM-pythia8/RunIISpring16MiniAODv2-PUSpring16_80X_mcRun2_asymptotic_2016_miniAODv2_v0_ext1-v1/MINIAODSIM	224.2
/DYJetsToLL_M-5to50_HT-200to400_TuneCUETP8M1_13TeV-madgraphMLM-pythia8/RunIISpring16MiniAODv2-PUSpring16_80X_mcRun2_asymptotic_2016_miniAODv2_v0_ext1-v1/MINIAODSIM	37.2
/DYJetsToLL_M-5to50_HT-600toInf_TuneCUETP8M1_13TeV-madgraphMLM-pythia8/RunIISpring16MiniAODv2-PUSpring16_80X_mcRun2_asymptotic_2016_miniAODv2_v0_ext1-v1/MINIAODSIM	1.124
Other datasets	
/WZTo3LNu_TuneCUETP8M1_13TeV-powheg-pythia8/RunIISpring16MiniAODv2-PUSpring16_80X_mcRun2_asymptotic_2016_miniAODv2_v0-v1/MINIAODSIM [62]	4.102

Table B.3: Cross sections of the T6bbllslepton process for different $\tilde{b}$ masses

$m_{\tilde{b}}$ [GeV]	σ [pb]
400	1.83537
425	1.312
450	0.9483
475	0.6971
500	0.5185
525	0.3903
550	0.2961
575	0.2261
600	0.1746
625	0.1364
650	0.1070
675	0.08449
700	0.06705
750	0.0431418
775	0.0348796
800	0.0283338
850	0.0189612
900	0.0128895
950	0.00883465

References

[1] **CMS** Collaboration, S. Chatrchyan *et al.*, "Observation of a new boson at a mass of 125 GeV with the CMS experiment at the LHC," *Phys. Lett. B* **716** (2012) 30–61, `arXiv:1207.7235`.

[2] **ATLAS** Collaboration, G. Aad *et al.*, "Observation of a new particle in the search for the Standard Model Higgs boson with the ATLAS detector at the LHC," *Phys. Lett. B* **716** (2012) 1–29, `arXiv:1207.7214`.

[3] **SLD Electroweak Group, DELPHI, ALEPH, SLD, SLD Heavy Flavour Group, OPAL, LEP Electroweak Working Group, L3** Collaboration, S. Schael *et al.*, "Precision electroweak measurements on the Z resonance," *Phys. Rept.* **427** (2006) 257–454, `arXiv:hep-ex/0509008`.

[4] A. Straessner, "Measurement of the W boson mass at LEP," in *Proceedings, 39th Rencontres de Moriond, 04 Electroweak interactions and unified theories: La Thuile, Aosta, Italy, Mar 21-28, 2004*, pp. 3–10. 2004. `arXiv:hep-ex/0405005`.

[5] **CMS** Collaboration, V. Khachatryan *et al.*, "Search for Physics Beyond the Standard Model in Events with Two Leptons, Jets, and Missing Transverse Momentum in pp Collisions at $\sqrt{s} = 8$ TeV," *JHEP* **04** (2015) 124, `arXiv:1502.06031`.

[6] **CMS** Collaboration, V. Khachatryan *et al.*, "Search for new physics in final states with two opposite-sign, same-flavor leptons, jets, and missing transverse momentum in pp collisions at $\sqrt{s} = 13$ TeV," *Submitted to: JHEP* (2016) , `arXiv:1607.00915`.

[7] **ATLAS** Collaboration, G. Aad *et al.*, "Search for supersymmetry in events containing a same-flavour opposite-sign dilepton pair, jets, and large missing transverse momentum in $\sqrt{s} = 8$ TeV pp collisions with the ATLAS detector," *Eur. Phys. J. C* **75** no. 7, (2015) 318, `arXiv:1503.03290`. [Erratum: Eur. Phys. J.C 75,no.10,463(2015)].

[8] **ATLAS** Collaboration, G. Aad *et al.*, "A search for Supersymmetry in events containing a leptonically decaying Z boson, jets and missing transverse momentum in $\sqrt{s} = 13$ TeV pp collisions with the ATLAS detector,". `http://inspirehep.net/record/1410175`.

[9] S. L. Glashow, "Partial Symmetries of Weak Interactions," *Nucl. Phys.* **22** (1961) 579–588.

[10] A. Salam and J. Ward, "Electromagnetic and weak interactions," *Physics Letters* **13** no. 2, (1964) 168 – 171.

[11] S. Weinberg, "A model of leptons," *Phys. Rev. Lett.* **19** (Nov, 1967) 1264–1266.

[12] S. F. Novaes, "Standard model: An Introduction," in *Particles and fields. Proceedings, 10th Jorge Andre Swieca Summer School, Sao Paulo, Brazil, February 6-12, 1999*, pp. 5–102. 1999. `arXiv:hep-ph/0001283`.

[13] S. Weinberg, "Effects of a neutral intermediate boson in semileptonic processes," *Phys. Rev. D* **5** (1972) 1412–1417.

[14] Particle Data Group, C. Patrignani, *et al.*, "Review of particle physics," *Chin. Phys. C* **40** (2016) 100001.

[15] P. W. Higgs, "Broken symmetries and the masses of gauge bosons," *Phys. Rev. Lett.* **13** (Oct, 1964) 508–509.

[16] F. Englert and R. Brout, "Broken symmetry and the mass of gauge vector mesons," *Phys. Rev. Lett.* **13** (Aug, 1964) 321–323.

[17] S. P. Martin, "A Supersymmetry primer," `arXiv:hep-ph/9709356`. [Adv. Ser. Direct. High Energy Phys.18,1(1998)].

[18] S. van den Bergh, "The Early history of dark matter," *Publ. Astron. Soc. Pac.* **111** (1999) 657, `arXiv:astro-ph/9904251`.

[19] W. Hu and S. Dodelson, "Cosmic microwave background anisotropies," *Ann. Rev. Astron. Astrophys.* **40** (2002) 171–216, `arXiv:astro-ph/0110414`.

[20] A. Del Popolo, "Nonbaryonic Dark Matter in Cosmology," *Int. J. Mod. Phys. D* **23** (2014) 1430005, `arXiv:1305.0456`.

[21] C. F. Kolda, "Gauge mediated supersymmetry breaking: Introduction, review and update," *Nucl. Phys. Proc. Suppl.* **62** (1998) 266–275, `arXiv:hep-ph/9707450`.

[22] **CMS** Collaboration, S. Chatrchyan *et al.*, "Interpretation of Searches for Supersymmetry with simplified Models," *Phys. Rev. D* **88** no. 5, (2013) 052017, `arXiv:1301.2175`.

[23] L. Evans and P. Bryant, "Lhc machine," *Journal of Instrumentation* **3** no. 08, (2008) S08001. `http://stacks.iop.org/1748-0221/3/i=08/a=S08001`.

[24] S. Myers, *The LEP Collider, from design to approval and commissioning.* John Adams' Lecture. CERN, Geneva, 1991. `http://cds.cern.ch/record/226776`. Delivered at CERN, 26 Nov 1990.

[25] P. Mouche, "Overall view of the LHC. Vue d'ensemble du LHC,". `https://cds.cern.ch/record/1708847`. General Photo.

[26] **ATLAS** Collaboration, G. Aad *et al.*, "The ATLAS Experiment at the CERN Large Hadron Collider," *JINST* **3** (2008) S08003.

[27] **CMS** Collaboration, S. Chatrchyan *et al.*, "The CMS experiment at the CERN LHC," *JINST* **3** (2008) S08004.

[28] **LHCb** Collaboration, A. A. Alves, Jr. *et al.*, "The LHCb Detector at the LHC," *JINST* **3** (2008) S08005.

[29] **ALICE** Collaboration, K. Aamodt *et al.*, "The ALICE experiment at the CERN LHC," *JINST* **3** (2008) S08002.

[30] "CMS public luminosity information: Peak luminosity per week in 2016." `https://twiki.cern.ch/twiki/bin/view/CMSPublic/LumiPublicResults`. Last accessed 24th Oct 2016.

[31] T. Sakuma and T. McCauley, "Detector and event visualization with sketchup at the CMS experiment," *Journal of Physics: Conference Series* **513** no. 2, (2014) 022032. `http://stacks.iop.org/1742-6596/513/i=2/a=022032`.

[32] **CMS** Collaboration, S. Chatrchyan *et al.*, "Performance of CMS muon reconstruction in pp collision events at $\sqrt{s} = 7$ TeV," *JINST* **7** (2012) P10002, `arXiv:1206.4071`.

[33] "38th international conference of high energy physics." `https://indico.cern.ch/event/432527/`, 2016.

[34] J. Alwall, R. Frederix, S. Frixione, V. Hirschi, F. Maltoni, O. Mattelaer, H.-S. Shao, T. Stelzer, P. Torrielli, and M. Zaro, "The automated computation of tree-level and next-to-leading order differential cross sections, and their matching to parton shower simulations," *JHEP* **07** (2014) 079, `arXiv:1405.0301`.

[35] J. Alwall *et al.*, "Comparative study of various algorithms for the merging of parton showers and matrix elements in hadronic collisions," *Eur. Phys. J. C* **53** (2008) 473–500, `arXiv:0706.2569`.

[36] S. Frixione, P. Nason, and C. Oleari, "Matching NLO QCD computations with Parton Shower simulations: the POWHEG method," *JHEP* **11** (2007) 070, `arXiv:0709.2092`.

[37] S. Alioli, P. Nason, C. Oleari, and E. Re, "A general framework for implementing NLO calculations in shower Monte Carlo programs: the POWHEG BOX," *JHEP* **06** (2010) 043, `arXiv:1002.2581`.

[38] P. Nason, "A New method for combining NLO QCD with shower Monte Carlo algorithms," *JHEP* **11** (2004) 040, `arXiv:hep-ph/0409146`.

[39] R. Placakyte, "Parton Distribution Functions," in *Proceedings, 31st International Conference on Physics in collisions (PIC 2011): Vancouver, Canada, August 28-September 1, 2011.* 2011. arXiv:1111.5452.

[40] T. Sjostrand, S. Mrenna, and P. Z. Skands, "A Brief Introduction to PYTHIA 8.1," *Comput. Phys. Commun.* **178** (2008) 852–867, arXiv:0710.3820.

[41] S. A. et al., "Geant4—a simulation toolkit," *Nuclear Instruments and Methods in Physics Research Section A: Accelerators, Spectrometers, Detectors and Associated Equipment* **506** no. 3, (2003) 250 – 303.

[42] A. Giammanco, "The fast simulation of the CMS experiment," *Journal of Physics: Conference Series* **513** no. 2, (2014) 022012. http://stacks.iop.org/1742-6596/513/i=2/a=022012.

[43] I. R. Kenyon, "The drell-yan process," *Reports on Progress in Physics* **45** no. 11, (1982) 1261. http://stacks.iop.org/0034-4885/45/i=11/a=002.

[44] G. Petrucciani, A. Rizzi, and C. Vuosalo, "Mini-aod: A new analysis data format for CMS," *Journal of Physics: Conference Series* **664** no. 7, (2015) 072052. http://stacks.iop.org/1742-6596/664/i=7/a=072052.

[45] R. Brun and F. Rademakers, "ROOT: An object oriented data analysis framework," *Nucl. Instrum. Meth. A* **389** (1997) 81–86.

[46] **CMS** Collaboration, F. Beaudette, "The CMS Particle Flow Algorithm," in *Proceedings, International Conference on Calorimetry for the High Energy Frontier (CHEF 2013): Paris, France, April 22-25, 2013*, pp. 295–304. 2013. arXiv:1401.8155. https://inspirehep.net/record/1279774/files/arXiv:1401.8155.pdf.

[47] T. Speer, K. Prokofiev, R. Fruhwirth, W. Waltenberger, and P. Vanlaer, "Vertex fitting in the CMS tracker,". http://inspirehep.net/record/711542/.

[48] E. Chabanat and N. Estre, "Deterministic annealing for vertex finding at CMS," in *Computing in high energy physics and nuclear physics. Proceedings, Conference, CHEP'04, Interlaken, Switzerland, September 27-October 1, 2004*, pp. 287–290. 2005. http://cds.cern.ch/record/865587/files/p287.pdf.

[49] **CMS** Collaboration, V. Khachatryan *et al.*, "Performance of Electron Reconstruction and Selection with the CMS Detector in Proton-Proton Collisions at $\sqrt{s} = 8$ TeV," *JINST* **10** no. 06, (2015) P06005, arXiv:1502.02701.

[50] "The electron/photon reconstruction for run2." https://indico.cern.ch/event/306030/. access CMS exclusive, last accessed 24th Oct 2016.

[51] W. Adam, R. Frühwirth, A. Strandlie, and T. Todorov, "Reconstruction of electrons with the gaussian-sum filter in the cms tracker at the lhc," *Journal of Physics G: Nuclear and Particle Physics* **31** no. 9, (2005) N9. http://stacks.iop.org/0954-3899/31/i=9/a=N01.

[52] **CMS** Collaboration, C. Collaboration, "Search for new physics in final states with two opposite-sign, same-flavor leptons, jets, and missing transverse momentum in pp collisions at $\sqrt{s} = 13$ TeV,". http://inspirehep.net/record/1479649.

[53] R. Frühwirth, "Application of kalman filtering to track and vertex fitting," *Nuclear Instruments and Methods in Physics Research Section A: Accelerators, Spectrometers, Detectors and Associated Equipment* **262** no. 2, (1987) 444 – 450.

[54] M. Cacciari, G. P. Salam, and G. Soyez, "The Anti-k(t) jet clustering algorithm," *JHEP* **04** (2008) 063, arXiv:0802.1189.

[55] M. Cacciari and G. P. Salam, "Dispelling the N^3 myth for the k_t jet-finder," *Phys. Lett. B* **641** (2006) 57–61, arXiv:hep-ph/0512210.

[56] M. Cacciari, G. P. Salam, and G. Soyez, "FastJet User Manual," *Eur. Phys. J. C* **72** (2012) 1896, arXiv:1111.6097.

[57] "Introduction to jet energy corrections at cms." https://twiki.cern.ch/twiki/bin/viewauth/CMS/IntroToJEC. Access CMS exclusive, last accessed 24th Oct 2016.

[58] **CMS** Collaboration, S. Chatrchyan *et al.*, "Identification of b-quark jets with the CMS experiment," *JINST* **8** (2013) P04013, arXiv:1211.4462.

[59] C. F. Berger, Z. Bern, L. J. Dixon, F. F. Cordero, D. Forde, T. Gleisberg, H. Ita, D. A. Kosower, and D. Maître, "Next-to-leading order qcd predictions for $w + 3$-jet distributions at hadron colliders," *Phys. Rev. D* **80** (Oct, 2009) 074036.

[60] **ATLAS** Collaboration, T. A. collaboration, "Search for new phenomena in events containing a same-flavour opposite-sign dilepton pair, jets, and large missing transverse momentum in $\sqrt{s} = 13$ TeV pp collisions with the ATLAS detector,". http://inspirehep.net/record/1487585/.

[61] J. M. Campbell, R. K. Ellis, P. Nason, and E. Re, "Top-pair production and decay at NLO matched with parton showers," *JHEP* **04** (2015) 114, arXiv:1412.1828.

[62] P. Nason and G. Zanderighi, "W^+W^- , WZ and ZZ production in the POWHEG-BOX-V2," *Eur. Phys. J. C* **74** no. 1, (2014) 2702, arXiv:1311.1365.